Calibration Probe Uncertainty and Validation for the Hypersonic Material Environmental Test System

Andrew J. Brune,* Thomas K. West IV, † and Laura M. White ‡
NASA Langley Research Center, Hampton, VA, 23681

This paper presents an uncertainty analysis of the stagnation-point calibration probe surface predictions for conditions that span the performance envelope of the Hypersonic Materials Environmental Test System facility located at NASA Langley Research Center. A second-order stochastic expansion was constructed over 47 uncertain parameters to evaluate the sensitivities, identify the most significant uncertain variables, and quantify the uncertainty in the stagnation-point heat flux and pressure predictions of the calibration probe for a low- and high-enthalpy test condition. A sensitivity analysis showed that measurement bias uncertainty is the most significant contributor to the stagnation-point pressure and heat flux variance for the low-enthalpy condition. For the high-enthalpy condition, a paradigm shift in sensitivities revealed the computational fluid dynamics model input uncertainty as the main contributor. A comparison between the prediction and measurement of the stagnation-point conditions under uncertainty showed that there was evidence of statistical disagreement. A validation metric was proposed and applied to the prediction uncertainty to account for the statistical disagreement when compared to the possible stagnation-point heat flux and pressure measurements.

Nomenclature

A	Cross-sectional area of the nozzle inlet (plenum), cm^2
C	Conversion coefficient in the bulk enthalpy energy balance, $6.315x10^{-5}$ min-m^3/s-gal
C_p	Specific heat based on constant pressure, J/kg-K
C_w	Cooling water flow rate, gal/min
c_i	Mass fraction of species i
D	Deterministic variable

d	Validation metric
E	Arc heater voltage, volts
F	Probability distributions of a prediction
H	Enthalpy, MJ/kg
H_o	Total enthalpy, MJ/kg
I	Arc heater current, amps
l	Length of the copper slug, cm
M_{total}	Total mass flow rate, kg/sec
n	Number of random dimensions
P	Pressure, kPa
P_{box}	Test cabin pressure, Pa
$\dot{q}$	Heat flux, W/cm^2
q	Polynomial expansion order
r	Radius from plenum centerline, cm
R	Response output variable
R_B	Base radius of the calibration probe, cm
R_N^{eff}	Effective nose radius of the calibration probe, cm
S	Probability distributions of an experimental measurement
T	Temperature, K
t	Time, sec
u	Axial velocity, m/sec
X	Axial distance from the nozzle inlet (plenum), cm
Z	Radial distance from the nozzle centerline, cm
Δ	Differential operator
Ψ	Random basis function
α	Polynomial expansion coefficient
ρ	Density, kg/m^3

ξ Random variable

Subscripts

CL Centerline of the plenum

CW Cooling water

Cu Copper

L Left probability box boundaries

R Right probability box boundaries

ref Reference condition

w Wall condition

I. Introduction

Uncertainties are generally present in the flow-field environment of arc-jet facilities. Of the limited number of facilities available to currently support thermal protection system (TPS) development and evaluation, arc-jet facilities can provide the most relevant aerothermal loads on material systems for durations sufficient to test over the total flight heat loads. Development of codes to model the TPS thermal response for various flight conditions, other than those within limited operating envelopes of ground facilities, is also supported by testing efforts. Determination and verification of appropriate arc-jet conditions and test model configurations is a challenge in the presence of uncertainties due to inherent variations in the measurements used to inform the computational fluid dynamics (CFD) models, while the modeling approach has model-form (epistemic) uncertainty due to lack of knowledge or incomplete information. Uncertainty quantification (UQ) is critical in the simulations to assess the accuracy of the results, and global sensitivity information for the output quantities of interest play an important role for ranking the contribution of each uncertainty source to the overall uncertainty. The sensitivity information can be used for the proper allocation of resources to improve the accuracy of the analysis and design process.

Computational fluid dynamics (CFD) analysis frameworks have been developed for NASA Ames arc-jet facilities, including the Aerodynamic Heating Facility (AHF) and the Interaction Heating Facility (IHF), using radial sweep

information to construct the inflow states [1]. Other arc-jet facilities, which include the Hypersonic Materials Environment Test System (HyMETS), have limited information from the stagnation probe measurements along the stagnation streamline and require reconstructive assumptions about the inflow state based on limited calibration data. A paper by Mazaheri [2] introduced a simple methodology for modeling HyMETS to determine the arc-jet flow conditions consistent with the lumped pressure and bulk enthalpy, assuming equilibrium theory through the nozzle. More recently, Brune et al. presented an approach to determine the non-uniform arc-jet flow profiles at the plenum, prior to the nozzle, and level of surface catalysis of the calibration probe that corresponds to the measured heat flux and pressure [3].

The objective of this study is to perform an uncertainty analysis of stagnation-point calibration probe surface predictions for multiple test conditions that span the performance envelope of HyMETS, subject to uncertainty sources in the CFD model and related inputs, such as catalytic recombination efficiency, and the facility measurements. The model approach from Brune et al. [3] is used. This consists of a direct simulation of the thermal nonequilibrium flow and its non-uniformity through the nozzle and test cabin, which is used to predict the conditions on a non-blowing copper surface probe. Two arc heater conditions, one at low bulk enthalpy and one at high bulk enthalpy, are evaluated to capture the performance envelope of the HyMETS facility. For both test conditions, a sensitivity analysis is performed to identify the uncertain variables that greatly influence the uncertainty in the surface predictions of the calibration probes, and recommended investment paths are discussed. The uncertainty in the surface probe predictions are presented and compared to the uncertainty in the probe measurements alone. A validation metric is proposed and applied to the prediction uncertainty if statistical differences between the data and predictions are observed. This study is an initial step to a more sophisticated uncertainty analysis that will be performed for an ablating/non-ablating TPS sample in the arc-jet facility.

This paper is organized to first present an overview of the HyMETS facility configuration and instrumentation in Section II. Section III presents the computational models used to establish the plenum flow profiles consistent with the inferred enthalpy that corresponds to the measured arc-jet heat flux and pressure. Section III also provides a summary of results for the low-enthalpy arc heater condition considered in this study, without any uncertainties, to demonstrate the modeling approach, followed by discussion of the uncertainty sources from the CFD model and measurements used to inform the CFD model. Section IV presents the uncertainty quantification methodology and the validation approach when comparing the statistical results of the calibration probe predictions and data. Section V presents the results of the

sensitivity analysis and compares the statistical results of the probe surface predictions to the measured calibration probe data for the low- and high-enthalpy conditions. Conclusions of this study are given in Section VI.

II. HyMETS Arc-jet Facility

Ground testing of the aerothermal environments of TPS over a range of flight-relevant conditions is needed for successful development and demonstration. Arc-jet facilities are typically used to test the TPS in flight-relevant heat flux, surface pressure, and shear force environments. In this study, the HyMETS facility at NASA Langley Research Center is considered to initially assess the uncertainty at two arc heater conditions that span the performance envelope with calorimetry. This study is an initial step to a more sophisticated anaysis that will be performed to assess the uncertainty at similar conditions for an ablating/non-ablating TPS specimen in the HyMETS facility. The history of the facility use can be found in the work by Splinter et al. [4], most of which includes material characterization for hypersonic vehicles [5–7].

The HyMETS facility uses a segmented-constrictor dc-electric arc heater as an arc heater generator with diatomic nitrogen, diatomic oxygen, and argon injected as the test gas. The arc heater generator can be visualized in Figure 1 and 2 and is mounted on the outside of the test cabin door. The generator consists of water-cooled components, which include a copper cathode with tungsten button emitter, electrically-isolated copper segment constrictors with a 1.27-cm diameter bore, and a copper divergent-ring anode. Test gasses are injected tangentially into the bore of the arc heater generator at six discrete locations and can be mixed at various levels to desired atmospheric composition. The gasses are heated by a high-voltage electric arc that is maintained between the cathode and anode to create a high-temperature dissociated flow. The HyMETS facility has a viewport on the test cabin door to obtain video and pyrometer thermal data of the test specimen, in addition to viewports in the test cabin walls. A detailed description and overview of the HyMETS facility and performance envelopes for stagnation testing can be found in the literature [4, 8].

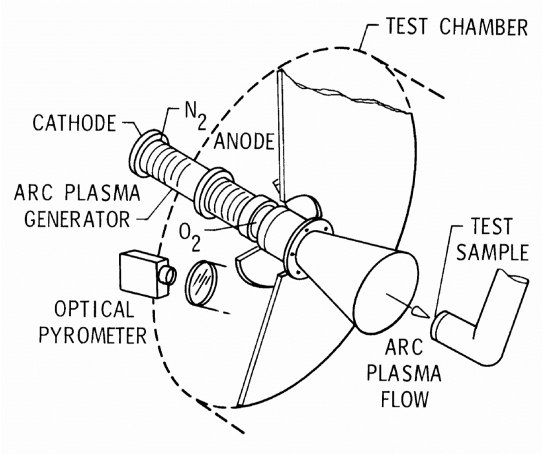

Fig. 1 HyMETS test setup schematic.

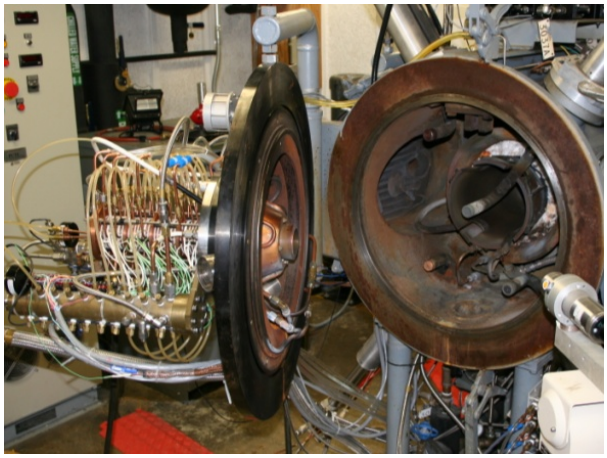

Fig. 2 HyMETS facility test setup.

For stagnation testing, a water-cooled 6.35-cm exit diameter conical nozzle with a 1.27-cm throat diameter and half angle of 8 degrees, made of copper and attached to the arc heater generator system, is used to provide the appropriate combination of heat flux and pressure at the probe surface. The high-temperature flow from the arc heater generator is accelerated through the nozzle and exhausted into a 60.9-cm wide by 91.4-cm long vacuum test cabin. The flow proceeds downstream of the test cabin into a collector cone, a 15.24-cm diameter constant cross-section diffuser, and a coiled-copper tubing heat exchanger to decelerate and cool the flow. The test cabin is pumped to the desired conditions with a mechanical pumping system. Test models are positioned on the centerline of the flow just downstream of the nozzle exit. A Pitot probe, a slug calorimeter, and a TPS specimen are injected in sequence into the flow during each run.

A flat-face Pitot probe and copper slug calorimeter [9, 10] in Figure 3 and 4, respectively, are used to determine the stagnation heat flux and surface pressure during each run. The Pitot probe and slug calorimeter are equivalently referred as the calibration probe in the remaining sections. The copper slug calorimeter is used to determine the cold-wall heat flux and consists of an un-cooled slug sensor element that is 1.27-cm diameter by 1.27-cm long with an uncooled shroud that is 3.3-cm diameter by 2.16-cm long and a flow-face edge radius of 0.318 centimeters. The slug sensor element and shroud are fabricated out of oxygen-free high-conductivity copper. The slug sensor element has a 0.005-cm wide "insulating" air gap between it and the shroud and is held in place using six cone-tipped set-screws. The slug sensor element also has a Type-K thermocouple mounted on its back surface to measure temperature rise. The length, diameter, and mass of the slug sensor element are measured prior to calorimeter assembly. The copper slug calorimeter is inserted into a steady-state flow for 2-3 seconds so that it achieves a backface temperature rise of several hundred degrees Fahrenheit, not to exceed a final temperature of 588 K (600^oF). The heat flux is calculated from the density of

the copper slug sensor element ρ_{Cu}, the temperature-dependent specific heat capacity of the element C_p, the length of the element l, and the slope of the temperature rise $\Delta T/\Delta t$ from the linear portion of the temperature response curve for the Type-K thermocouple using [9]:

$$\dot{q}_w = \rho_{Cu} C_{p_{Cu}} l \left(\frac{\Delta T_{Cu}}{\Delta t} \right) \tag{1}$$

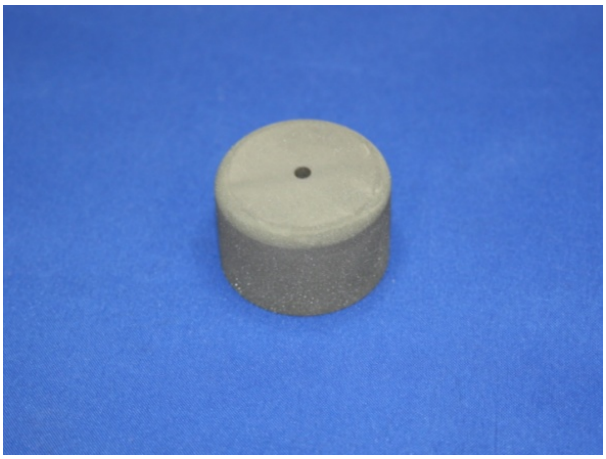

Fig. 3 Pitot tube.

Fig. 4 Copper slug calorimeter.

In addition to the surface pressure and heat flux, conditions in the arc jet are measured, including plenum total pressure downstream of the arc heater, prior to the nozzle, total mass flow rate, and the average bulk enthalpy at the nozzle exit. An energy balance is performed on the arc heater generator in HyMETS to calculate the bulk enthalpy. The energy input to the arc heater generator is determined by the product of voltage, E, and current, I, measurements. The energy removal from the arc heater generator is determined by the product of the cooling water flow rate C_W, and the differential temperature measured across the inlet and outlet of the cooling water manifolds, ΔT_{CW}. Finally, the energy that remains in the arc heater generator is divided by the total measured mass flow rate of the test gases, M_{total}. The bulk enthalpy is calculated using Eq. (2) [11]:

$$H_{bulk} = \frac{EI - CC_W C_{p_{CW}} \rho_{CW} \Delta T_{CW}}{M_{total}} \tag{2}$$

The constant C converts the energy output in the second term to the proper units.

III. Computational Models and Uncertainty Sources

In this section, the computational modeling process is first presented to estimate the plenum profiles given a unique set of arc heater conditions without uncertainty applied. The calibration probe predictions are then shown and compared to the measured data to demonstrate the need to assess the uncertainty in the predictions and measured data, determine if there is statistical agreement, and apply a validation metric to account for any statistical differences. Finally, uncertainty sources are identified and discussed in the last subsection.

A. Computational Modeling Approach

The Langley Aerothermodynamic Upwind Relaxation Algorithm (LAURA-5) CFD code is used to compute the flow-field and surface environments of the HyMETS facility. In the CFD simulations, the arc-jet flow field was modeled with 6-species gas (N_2, O_2, NO, N, O, Ar) for the low-enthalpy condition and 13-species gas (N_2, O_2, NO, N, O, Ar, N_2^+ ,O_2^+, NO^+, N^+, O^+, Ar^+, e^-) for the high-enthalpy condition. These conditions are similar to those reported by Brune et al [3]. Thermodynamic nonequilibrium is modeled using two energy equations: one for the translational and rotational modes of internal energy and the other for the vibrational and electronic modes [12]. The calibration probes (Pitot tube and slug calorimeter) are assumed to be at an isothermal cold-wall temperature of 300 K. (Note that the probes are injected for calibration for only a few seconds as discussed in Section II.) The transport and thermodynamic properties in the flow-field environment are computed from species collision integrals [13–15] and curve fit data [16], respectively. Further details on the flow solver and previous applications can be found in the literature [17–24].

An axisymmetric computational grid used in this study consists of four structured blocks (Figure 5). The blocks together form a structured mesh that spans the nozzle and surrounding flow around the calibration probes in the test cabin. A grid convergence study showed that 257 surface normal cells and wall spacing on the order of 10^{-5} was sufficient for reliable heating and pressure predictions on the calibration probes. As shown in Figure 5, viscous surfaces are applied on the nozzle and calibration probe surfaces. Non-uniform plenum profiles are used for boundary conditions on the inflow boundary of the nozzle.

The enthalpy profile at the plenum is first estimated using the measured plenum total pressure and inferred enthalpy computed from the measured surface heat flux and pressure. Equilibrium theory is used to estimate the initial plenum profile conditions for the nonequilibrium CFD, which was then used to compute the inferred enthalpy and the enthalpy

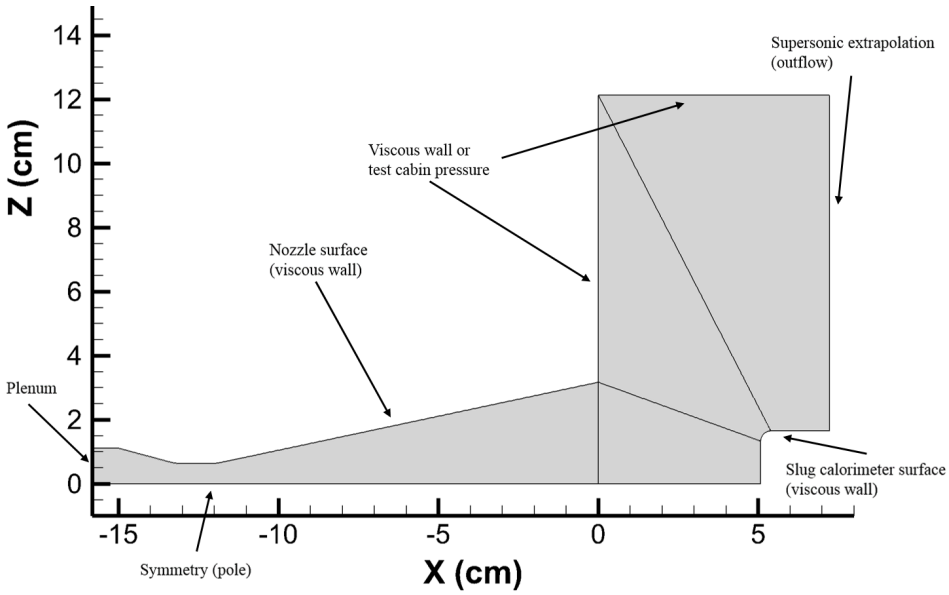

Fig. 5 Computational grid layout for arc-jet CFD flow simulations.

profile at the nozzle exit. The enthalpy profile at the plenum is assumed to have a parabolic shape in mathematical form of Eq. (3):

$$H(r) = a_0 + a_1 r + a_2 r^2 \tag{3}$$

subject to

$$H(0) = H_{CL}^{guess} \tag{4}$$

$$\left.\frac{dH}{dr}\right|_{r=0} = 0 \tag{5}$$

$$\frac{1}{A}\iint_A H(r) = H_{bulk} \tag{6}$$

In Eq. (3), $H(r)$ is the enthalpy profile defined at the plenum and varies with radius r from the nozzle centerline. The coefficients are determined by the conditions from Eq. (4)-(6), where the centerline enthalpy defines the leading coefficient, a_0, the maximum (peak) enthalpy at the centerline defines coefficient, a_1, and the bulk enthalpy at the plenum

defines coefficient, a_2. Given the measured plenum total pressure and enthalpy profile, the remaining thermodynamic state profiles (species mass fractions, temperature, and density) can be determined assuming thermochemical equilibrium at the plenum. The measured mass flow rate that corresponds to the arc-jet pressure and bulk enthalpy can be used to estimate the plenum velocity profile.

The inferred enthalpy predicted by CFD at the nozzle exit is compared to the inferred enthalpy corresponding to the measured heat flux and pressure by the calibration probe. The inferred enthalpy is estimated using an engineering correlation that is a function of the measured probe surface values [25]:

$$H_{inferred} = \frac{2.82\dot{q}_w}{(P_w/R_N^{eff})^{1/2}} + H_w \tag{7}$$

$$R_N^{eff} = 3.33R_B \tag{8}$$

In Eq. (7), R_N^{eff} is an effective hemispherical nose radius corresponding to the calibration probe base diameter, R_B. The effective nose radius is estimated using Eq. (8) [26, 27]. The leading coefficient provides a reasonable estimate of the effective nose radius based on stagnation point results for various corner-to-base radius ratios [2]. Furthermore, the wall enthalpy, H_w, is typically considered negligible for an isothermal cold-wall condition. If needed, adjustments in the enthalpy profile at the plenum are made to match the estimated inferred enthalpy from Eq. (7).

B. Arc-jet Flow-field Environment

In the previous subsection, the methodology to estimate the arc-jet plenum profiles prior to the conical nozzle was presented. Examples of the plenum profiles are shown in Figure 6(a) and 6(b) for the low-enthalpy condition with an arc-jet bulk enthalpy and plenum total pressure of 5.5 MJ/kg and 103 kPa, respectively. These conditions correspond to the calibrated values tested on the 3.3-cm calibration probe at a surface pressure and heat flux of about 4.3 kPa and 56.7 W/cm^2, respectively. For this condition, the flow temperature profile is fairly uniform and peaks on the centerline at about 3500 K, which corresponds to a small amount of dissociated O_2. A negligible amount of N_2 dissociation is observed at this condition.

Figure 7 shows an illustration of the computed nozzle and test cabin flow field. The flow expands in the nozzle to around Mach 5 at the exit with a computed inferred enthalpy of about 5.7 MJ/kg. Comparing the inferred enthalpy

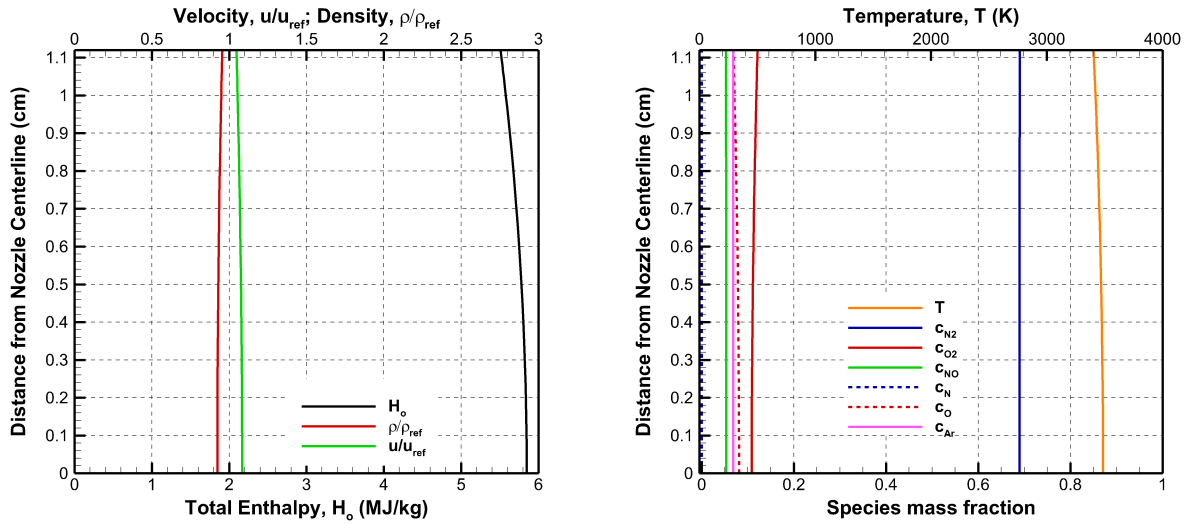

(a) Density, velocity, and total enthalpy.

(b) Species composition, temperature, and total enthalpy.

Fig. 6 Estimated plenum profiles for the 5.5 MJ/kg bulk enthalpy, 103 kpa total plenum pressure condition: 6.35-cm nozzle flow, parabolic enthalpy profile.

prediction from CFD to the estimated inferred enthalpy from Eq. (7), the plenum centerline enthalpy is verified to correspond with the inferred enthalpy that matches the appropriate combination of measured heat flux and surface pressure. In the nozzle, the chemical composition freezes near the throat where the dissociated gas mixture is vibrationally excited. As expected, the computations predict that the flow is chemically and vibrationally frozen before it reaches the nozzle exit, which is shown in Figure 7(d). Coincidentally, the vibrational and translational temperatures in Figure 7(c) deviate from equilibrium near the nozzle throat as well. Oxygen remains partially dissociated within the entire flowfield, except in the boundary layer near the walls, while nitrogen remains in its molecular state.

Figure 8 shows predicted pressure and heat flux for the 3.3-cm calibration probe. The profiles are shown along the calibration probe surface at radial distance, Z, from the center of the probe. The figure on the left shows the predicted pressure distribution. The CFD results predicted for the heat flux on the calibration probe surface are shown on the right. The predicted heat flux and pressure values at the stagnation point (or center) of the calibration probes are compared to the measured values. The results shown assume a 10% catalytic recombination efficiency in promoting atomic species to recombine at the copper surface. As indicated in Figure 8, there is roughly 15-20% disagreement between the measured data and the model prediction based on the unique set of arc heater conditions. These errors appear to be large at first glance due to the tenous assumptions about the deterministic nature of the CFD model, the data used to inform the CFD model (e.g., arc heater and calibration probe data), and the catalytic behavior of the presumed copper surfaces of the

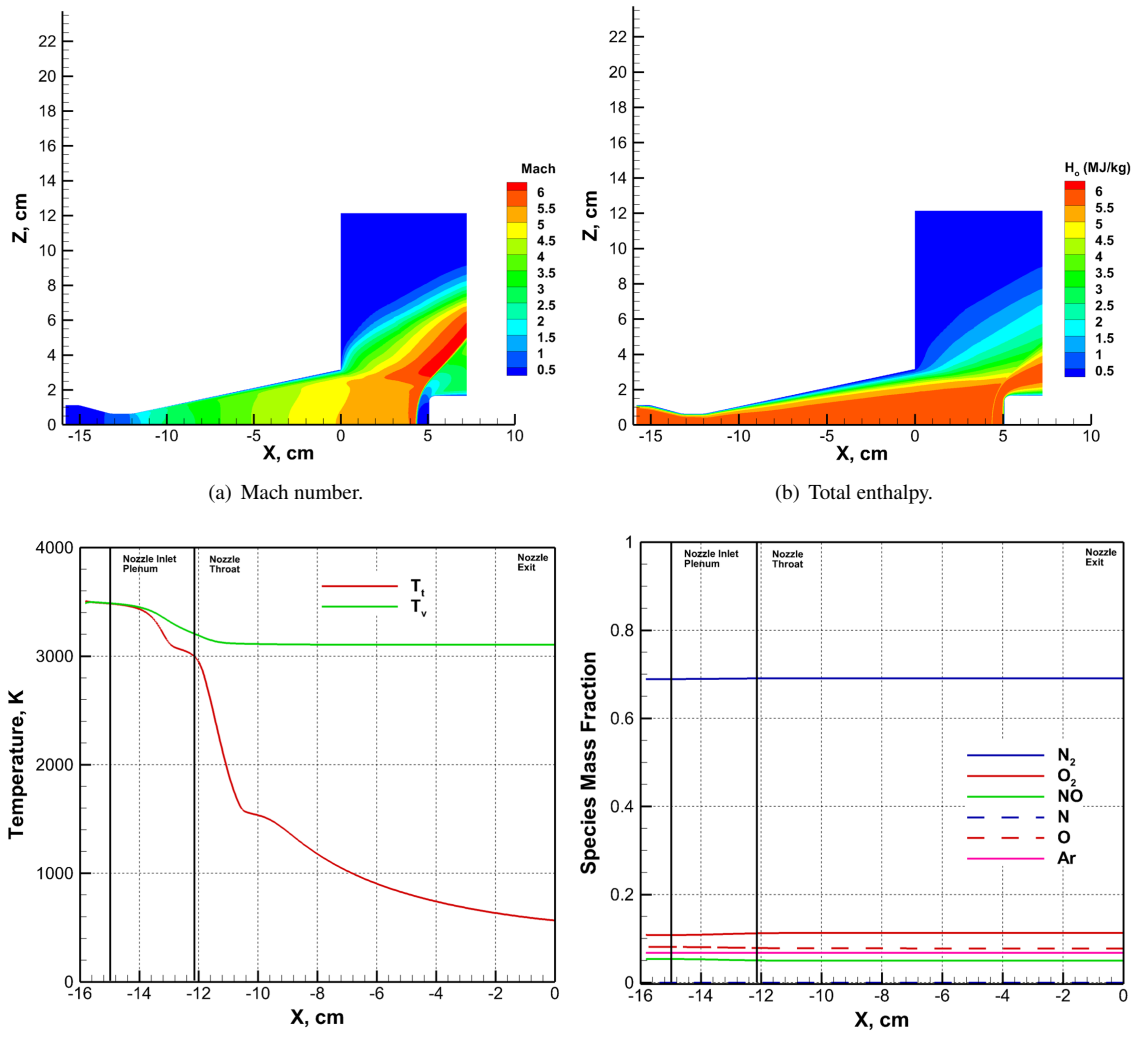

(a) Mach number.

(b) Total enthalpy.

(c) Nozzle centerline temperatures.

(d) Nozzle centerline species composition.

Fig. 7 Computed 6.35-cm nozzle flow field including the test cabin and 3.3-cm calibration probe for the 5.5 MJ/kg bulk enthalpy, 103 kpa total plenum pressure condition.

nozzle and calibration probe. Therefore, there is an imperative need to account for the probabilistic and model-form uncertainties and propagate them through the model process to determine whether there is statistical agreement between the predicted and measured calibration probe data.

C. Sources of Uncertainty

In this subsection, the sources of uncertainty are presented that will be propagated through the CFD model. Each section that follows discusses the rationale for including or eliminating each source of uncertainty. At the end of this section, a summary of all uncertainty sources will be given to detail the uncertain parameters, associated classification, and other relevant information.

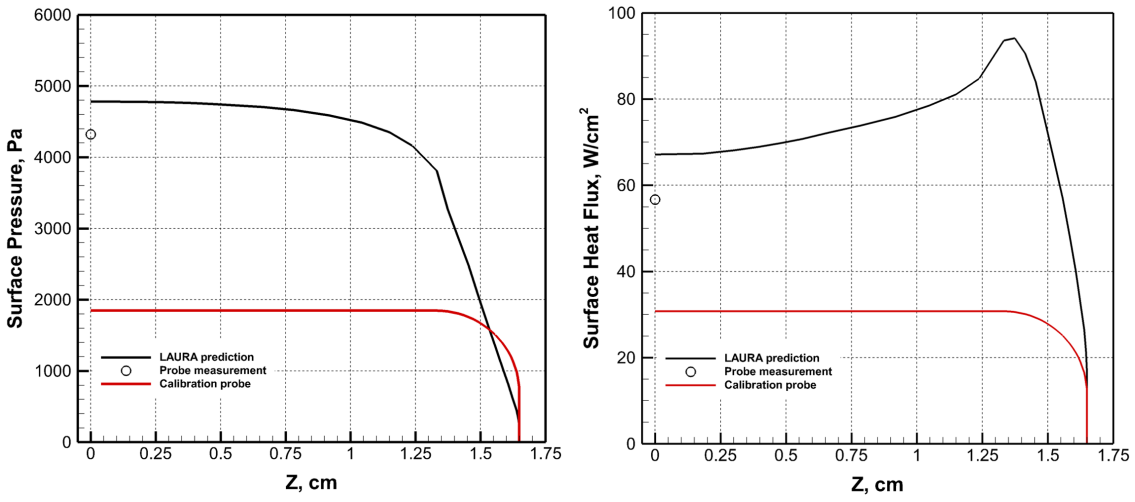

(a) Surface pressure.

(b) Convective heat flux.

Fig. 8 Computational results for the 5.5 MJ/kg bulk enthalpy, 103 kpa total plenum pressure condition tested on the 3.3-cm calibration probe.

1. HyMETS Measurements

HyMETS facility instrument data is collected by the data acquisition system at a frequency rate of 1000 Hz to sufficiently monitor the variations in the measurements. The actual measured value of an instrument can be written as

$$M = M_P + B \tag{9}$$

where M_P is the measurement subject to precision error due to random noise and B is the bias error of an instrument associated with the calibration to a standard. The uncertainty in the actual measurement M is subject to uncertainty in the precise measurement M_P and bias error B. In the case of the precision error, 214,000 data points from the acquisition system are used to determine the appropriate probabilistic distribution for most of the measurements, including arc heater settings (voltage and current), arc water flow rate, arc water temperature change, and injected gas flow rates. The data showed that the precision of these measurements follow a normal distribution estimated by the sample mean and standard deviation. The data for the total pressure measured at the plenum follow a uniform distribution.

The determination of the appropriate probabilistic distributions to model the precision uncertainty of the measurements required data collection at relevant arc heater times in which the measurements were stable. Statistical inspection of the sample set of each measurement at these relevant times were then conducted to evaluate whether sufficient data was available to assign an appropriate distribution with relevant statistical parameters. As an example, the stagnation

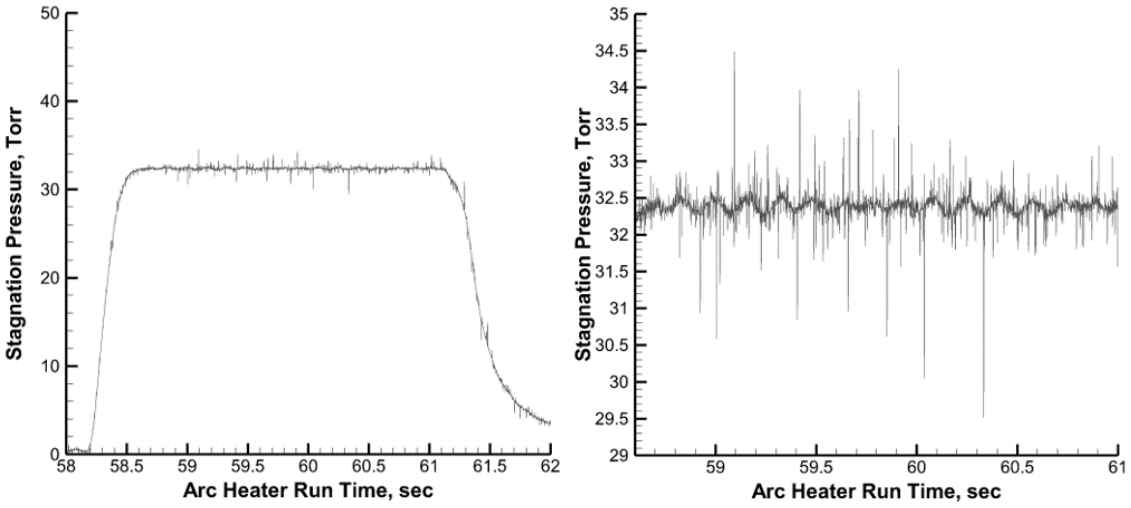

(a) Probe inserted in flow.

(b) Stable response.

Fig. 9 Stagnation pressure recorded at 1000 Hz for the 5.5 MJ/kg bulk enthalpy, 103 kpa total pressure condition.

pressure data for the low-enthalpy condition was recorded for a short period of time during the run in the arc-jet facility with a stable response for about 2.5 seconds (Figure 9). A total of 2,400 data points were observed for the stagnation pressure of the calibration probe during this stable period. Figure 10 shows the data from the stagnation pressure measurement follows a normal distribution, which can be sufficiently estimated by the sample mean and standard deviation in Figure 11 with the 2,400 data points available.

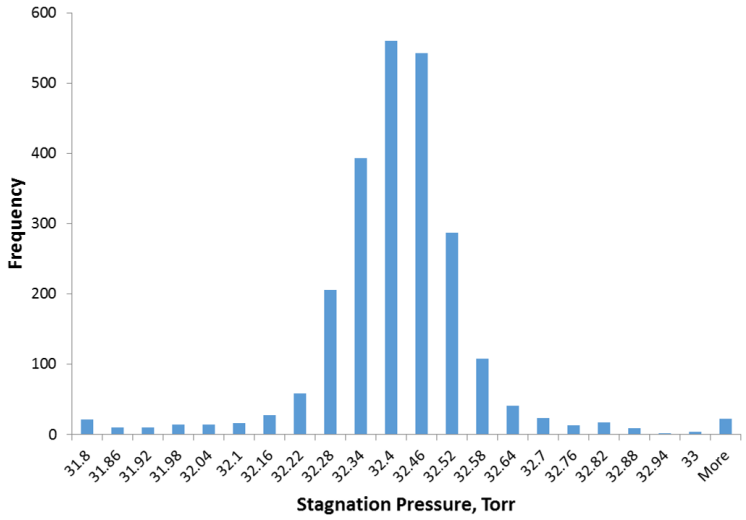

Fig. 10 Histogram of the stable stagnation pressure measurement for the 5.5 MJ/kg bulk enthalpy, 103 kpa total pressure condition.

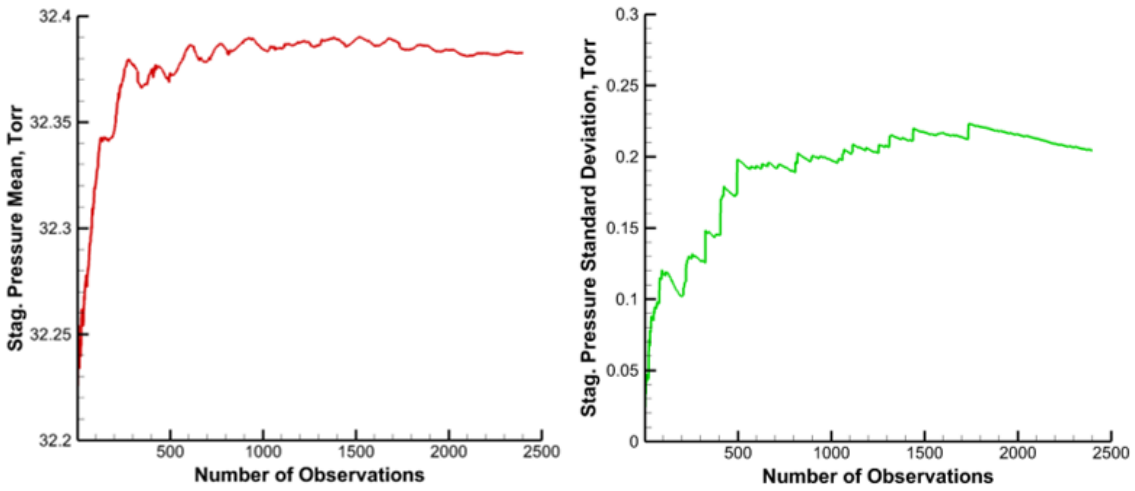

(a) Sample mean.

(b) Sample standard deviation.

Fig. 11 Convergence of the sample mean and standard deviation for the stable stagnation pressure measurement.

For the heat flux measurement from the slug calorimeter, the American Society for Testing and Materials (ASTM) standard test method assumes a one-dimensional heat transfer calculation of the heat flux measurement with no thermal losses and perfectly-insulated side boundaries of the slug [9]. Nawaz and Santos assessed the two-dimensional thermal environment of the slug calorimeter, while accounting for thermal losses, and provided an estimate of 10% uncertainty in heat flux measurement due to negligible thermal losses in the one-dimensional heat transfer technique from the ASTM standard and error in the instrumentation [10]. This study adopts this model-form uncertainty in the heat flux measurement as an epistemic uncertain variable.

The total biased error of a measurement is based on the bias error associated with individual measurements, B_n, in the data line path:

$$B = B_1 + B_2 + \ldots + B_n \tag{10}$$

In Eq. (10), n is the number of instruments in the data line path. The data line path begins with the measurement, e.g., heat flux transducer, pressure transducer, mass flow controllers, proceeds through any signal processing and/or electronics, and finally, reaches the data acquisition system. Individual bias errors are typically reported by the manufacturer as a percentage of the instrument full-scale range. Because there is insufficient data or lack of knowledge

in regards to the probabilistic representation of the bias uncertainty in the measurement, the total bias uncertainties are treated as epistemic uncertain variables.

2. Surface Catalysis

The catalytic wall recombination efficiency is a CFD physical model input that informs the surface catalytic property of the materials considered and can strongly affect the convective heat transfer to the surface. Nawaz et al. [28] reported a list of past experimental studies of catalycity and deduced catalytic efficiency values for copper probes in arc-jet facilities. The TPS community typically assumes the copper calorimeters to be fully-catalytic if the copper is in an oxgyen-free environment. According to studies discussed by Nawaz et al. [28], the copper surface can oxidize within minutes, or even seconds, to form cuprous or cupric oxide in a room temperature molecular oxygen environment. In addition, studies have shown that cuprous or cupric oxide forms on the surface during arc-jet tests involving some level of oxygen, where the copper probe exhibits some discoloration. A previous study by Brune et al. showed that a moderate catalytic recombination efficiency close to 10% for the oxygen atom, not the typical fully-catalytic assumption, agreed better with the probe heat flux measurement for a similar low-enthalpy condition in HyMETS [3]. This study adopts the uncertainty in catalytic efficiency to reflect values reported by Nawaz et al. [28] for several arc-jet tests, which range from the fully-catalytic condition as the upper limit and to as much as half of an order of magnitude variability below the nominal 10% recombination efficiency level.

3. CFD Model

The uncertainty in the convective heating to the surface of the calibration probe can be significant due to the chemical reaction processes in the flow. While difficult to measure, chemical kinetic rates have been shown to be significant in the calculation of species presence in the flow, which affects the recombination processes near the surface of the probe. For a 6-species gas, a total of five chemical reaction rates, including dissociation and exchange of species, are considered as sources of uncertainty. Studies by West et al. [18] and Johnston and Panesi [29] have treated the chemical kinetic rates as uncertain through the following implementation. The reaction rates of the ith reaction are governed by an Arrhenius expression of the form

$$k_{f,i} = A_{f,i} T_{f,i}^{n_{f,i}} exp(-D_{f,i}/T_i) \tag{11}$$

where $A_{f,i}$, $D_{f,i}$, and $n_{f,i}$ are parameters defined by West et al. [18] and Johnston and Panesi [29] for each dissociation/exchange reaction and T_i is the translational temperature. The leading coefficient $A_{f,i}$ is treated as an epistemic uncertain variable with lack of sufficient data for appropriate probabilistic implementation of these parameters in the CFD physical model. The kinetic rates can vary as much as an order of magnitude above or below the nominal value.

The uncertainty in the binary collision integrals can also be important in the convective heating at the probe surface and are treated as epistemic uncertainties due to lack of data required for appropriate probabilistic treatment. A study by Wright et al. [14] indicates that there can be as much as 30% uncertainty associated with integral curve fits of the collision pairs. Published work by Bose and Wright [30], Palmer [31], and Bose et al. [32] have treated the binary collision integrals as uncertain. For a 6-species gas, the collision integrals for only the neutral species interactions are taken to be uncertain. With six neutral species, there are 21 possible collision pairs that must be considered as sources of uncertainty in the integral curve fits. The uncertainty in binary collision integrals are implemented through the use of a leading coefficient factor, A, similar to the studies by Brune et al. [17] and Bose and Wright [30]:

$$\Omega^{1,1} = A f_1(T) \tag{12}$$

$$\Omega^{2,2} = A f_2(T) \tag{13}$$

The functions f_1 and f_2 are curve fit expressions as a function of flow temperature T, and the form of the curves fits are similar to those by Gupta et al. [13] In Eq. (12) and (13), $\Omega^{1,1}$ and $\Omega^{2,2}$ are used to calculate the diffusion coefficients, viscosity, and thermal conductivity.

4. Plenum Enthalpy Profile Shape

The impact of the plenum enthalpy profile shape on the surface environments of the calibration probe was analyzed. Recall from Section III.B that a parabolic enthalpy profile is assumed to model the behavior of the enthapy based on the estimated indicators of the bulk enthalpy and inferred enthalpy. The choice of analytically-modeled profiles for the enthalpy is heuristic based upon flow non-uniformity measurements in the arc-jet facility, which is limited to data at the stagnation line and bulk properties of the flow for HyMETS. Using specified total enthalpy profiles in Figure

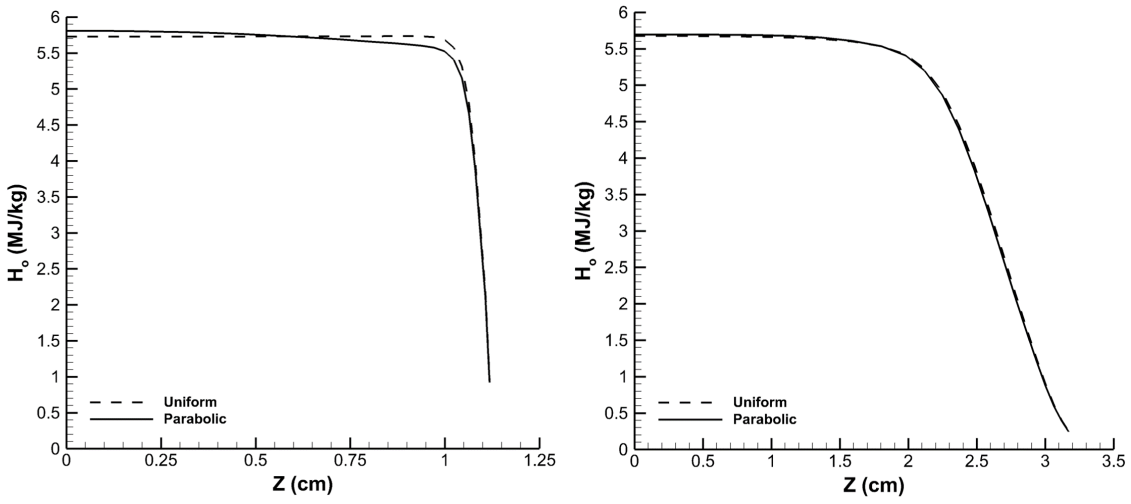

(a) Plenum. (b) Nozzle exit.

Fig. 12 Sample profiles of total enthalpy at the plenum and nozzle exit for the 5.5 MJ/kg bulk enthalpy, 103 kpa total plenum pressure condition.

12(a) and the plenum total pressure of approximately 103 kpa, non-equilibrium CFD calculations were performed to compute the resulting nozzle exit total enthalpy profiles. Figure 12(b) shows the total enthalpy profiles at the nozzle exit that correspond to the uniform and parabolic plenum enthalpy profiles. Despite the variability in the inflow profile shape of the enthalpy at the plenum, although small in this case, the results suggest that the flow is fully-developed at the nozzle exit with minor differences at the boundary layer edge. To investigate this further, Figure 13 compares the surface pressure and heat flux profiles around the calibration probe for each profile shape. The x-axis shows the radial distance, Z, measured from the center to the edge of the calibration probe. The solid red line represents the calibration probe surface for reference to the surface pressure and heat flux profiles. The enthalpy profile shape appears to have negligible impact on the surface conditions of the calibration probe, and as a result, has been eliminated as a source of uncertainty. These observations were also seen for a similar condition in Brune et al. [3] that exhibited more peaking of the flow with a much higher inferred enthalpy compared to the bulk (average) enthalpy.

5. Test Cabin Pressure

The impact of the test cabin pressure on the surface environments of the calibration probe was investigated. Brune et al. showed that the axial and radial velocities do not appear to be impacted by the change in cabin pressure within 2 cm of the nozzle centerline [3]. Therefore, it is expected that the flow expansion will not impact the surface pressure and heat flux profiles based on the size of the calibration probe considered in this study. This can be verified by comparing

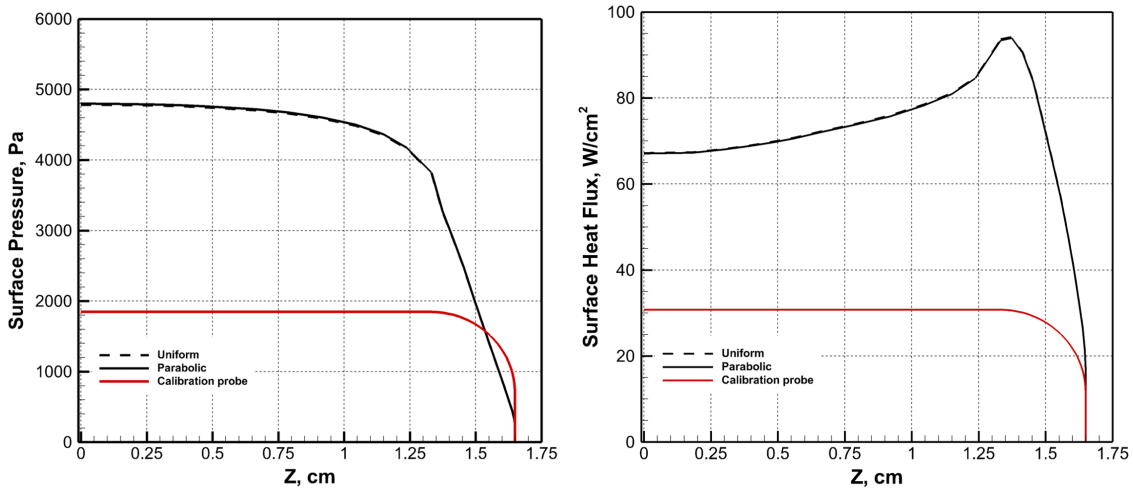

(a) Surface pressure.

(b) Convective heat flux

Fig. 13 Computed heat flux and pressure profiles along the calibration probe surface at multiple sample plenum enthalpy profiles in Figure 12.

the computed surface profiles of the calibration probe in Figure 14 for cabin pressures near vacuum and 228 Pa. In this figure, there are minor differences between the surface heat flux and pressure profiles at the 15 and 228 Pa cabin pressure. Therefore, a test model or probe with no more than 4-cm diameter has minimal impact from the unsteady effects of the free-jet expansion in the test cabin. Because the calibration probe is smaller than this threshold, the test cabin pressure has been eliminated as a source of uncertainty.

6. Summary of Uncertainty Sources

The previous subsections discussed the sources of uncertainty in the computational simulations of the HyMETS arc-jet facility, including those that were eliminated following impact studies on surface heating and pressure of the calibration probe. In summary, a total of 47 uncertainty variables are included in the uncertainty analysis of the surface probe predictions for the low- and high-enthalpy arc heater conditions. Tables 1 and 2 provide a list of the uncertain variables and associated uncertainty information, respectively. For the epistemic uncertain variables, the uncertain ranges are reported as varying from the corresponding nominal values. The uncertainty values for the uniformly- and normally-distributed variables are given as the bounded range and standard deviation, respectively. In Table 1 and 2, 'om' is denoted as order of magnitude, and 'sd' is the abbreviation for standard deviation.

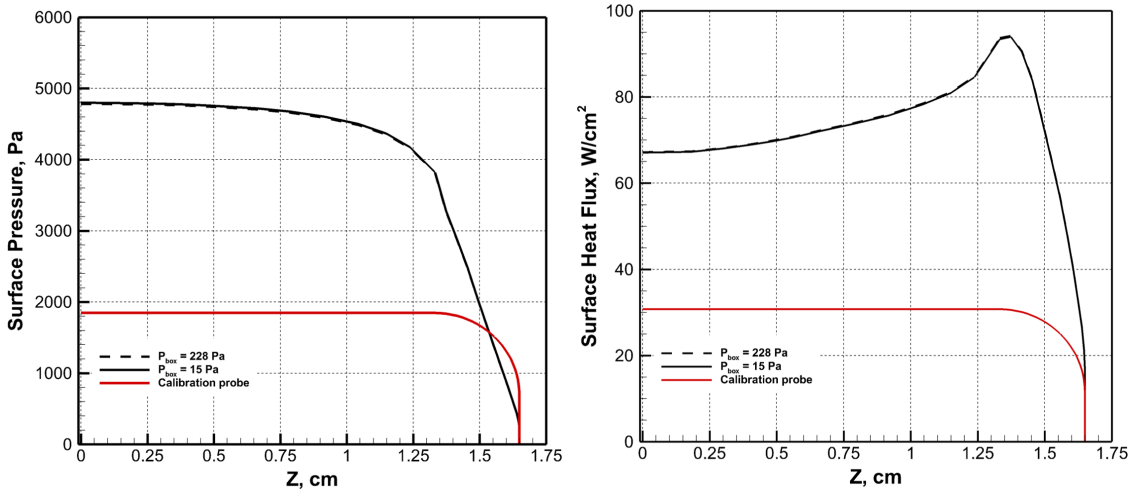

(a) Surface pressure.

(b) Convective heat flux.

Fig. 14 Computed heat flux and pressure profiles along the calibration probe surface at multiple cabin pressures for the 5.5 MJ/kg bulk enthalpy, 103 kpa total plenum pressure condition.

IV. Uncertainty Quantification and Validation Approach

This section outlines the uncertainty quantification and validation approach used in this study. As shown in Table 1 and 2, both aleatory and epistemic uncertainty sources exist in the computational model. This requires the use of a second-order uncertainty analysis approach, as described by Eldred and Swiler [33]. Given the computational expense of the model, a traditional sampling-based approach to forward uncertainty propagation was not feasible. An alternative surrogate-based approach was applied based on non-intrusive polynomial chaos, which is described next. Then, a description of the validation metric used to measure the model-form uncertainty is described in detail in the second subsection.

A. Non-intrusive Polynomial Chaos

Polynomial chaos is a surrogate modeling technique based on a spectral representation of the uncertainty [33]. An important aspect of spectral representations is the decomposition of a response value or random function R into a linear combination of separable deterministic and stochastic components, as shown in Eq. (14) for a polynomial of order q and dimension n.

$$R(\boldsymbol{D}, \boldsymbol{\xi}) \approx P_{q,n} = \sum_{i=0}^{N_t - 1} \alpha_i(\boldsymbol{D}) \Psi_i(\boldsymbol{\xi}) \tag{14}$$

Table 1 Uncertainty sources and relevant information for the the 5.5 MJ/kg bulk enthalpy, 103 kpa total pressure condition with a 3.3-cm calibration probe.

No.	Description	Classification	Nominal	Uncertainty	Ref.
1	Dissociation reaction rate: N_2 + M ↔ 2N + M	Epistemic	1	±1 om	
2	Dissociation reaction rate: NO + M ↔ N + O + M	Epistemic	1	±1 om	
3	Dissociation reaction rate: O_2 + M ↔ 2O + M	Epistemic	1	±50%	West and Johnston [18]
4	Exchange reaction rate: N_2 + O ↔ NO + N	Epistemic	1	±50%	
5	Exchange reaction rate: O_2 + N ↔ NO + O	Epistemic	1	±1 om	
6	Binary collision integral: N_2-N_2	Epistemic	1	±20%	
7	Binary collision integral: N_2-O_2	Epistemic	1	±20%	
8	Binary collision integral: N_2-NO	Epistemic	1	±25%	
9	Binary collision integral: N_2-N	Epistemic	1	±20%	
10	Binary collision integral: N_2-O	Epistemic	1	±20%	
11	Binary collision integral: N_2-Ar	Epistemic	1	±20%	
12	Binary collision integral: O_2-O_2	Epistemic	1	±20%	
13	Binary collision integral: O_2-NO	Epistemic	1	±25%	
14	Binary collision integral: O_2-N	Epistemic	1	±25%	
15	Binary collision integral: O_2-O	Epistemic	1	±20%	Wright et al. [14]
16	Binary collision integral: O_2-Ar	Epistemic	1	±20%	Palmer [31]
17	Binary collision integral: NO-NO	Epistemic	1	±20%	
18	Binary collision integral: NO-N	Epistemic	1	±25%	
19	Binary collision integral: NO-O	Epistemic	1	±25%	
20	Binary collision integral: NO-Ar	Epistemic	1	±25%	
21	Binary collision integral: N-N	Epistemic	1	±5%	
22	Binary collision integral: N-O	Epistemic	1	±5%	
23	Binary collision integral: N-Ar	Epistemic	1	±20%	
24	Binary collision integral: O-O	Epistemic	1	±20%	
25	Binary collision integral: O-Ar	Epistemic	1	±20%	
26	Binary collision integral: Ar-Ar	Epistemic	1	±5%	
27	Nozzle catalytic recombination efficiency: O	Epistemic	1	-0.5, +1 om	Nawaz et al. [28]
28	Calibration probe catalytic recombination efficiency: O	Epistemic	1	-0.5, +1 om	
29	Arc heater current precision (amps)	Normal	100	2.1 sd	
30	Arc heater current bias error (amps)	Epistemic	0	±0.4	
31	Arc heater voltage precision (amps)	Normal	586	4.8 sd	
32	Arc heater voltage bias error (amps)	Epistemic	0	±2	
33	Plenum total pressure precision (kpa)	Uniform	103	±0.5	
34	Plenum total pressure bias error (kpa)	Epistemic	0	±0.3	
35	Arc water flow rate precision (gpm)	Normal	30.4	0.1 sd	
36	Arc water flow rate bias error (gpm)	Epistemic	0	±0.4	
37	Arc water temperature change precision (F)	Normal	2.37	0.4 sd	HyMETS calibration data
38	Arc water temperature change bias error (F)	Epistemic	0	±0.4	and instrument specs
39	Molecular nitrogen flow rate precision (slpm)	Normal	299	0.7 sd	
40	Molecular nitrogen flow rate bias error (slpm)	Epistemic	0	±6	
41	Molecular oxygen flow rate precision (slpm)	Normal	83.8	0.9 sd	
42	Molecular oxygen flow rate bias error (slpm)	Epistemic	0	±1.5	
43	Argon flow rate precision (slpm)	Normal	15.7	0.4 sd	
44	Argon flow rate bias error (slpm)	Epistemic	0	±0.5	
45	Calibration probe stagnation pressure precision (kpa)	Normal	4.32	0.01 sd	
46	Calibration probe stagnation pressure bias error (kpa)	Epistemic	0	±0.008	
47	Calibration probe stagnation heat flux bias (W/cm^2)	Epistemic	56.7	±10%	Nawaz and Santos [10]

Here, α_i is the deterministic component and Ψ_i is the random variable basis functions corresponding to the i^{th} mode. The basis functions, Ψ_i, of each random variable are determined using the Askey key [34] and are dependent on the distribution of each random variable. The response, R, is a function of independent, deterministic variables, $\mathbf{D}$, and n independent, standard random variables, $\boldsymbol{\xi}$. Note that this series is, by definition, an infinite series; however, in practice, it is truncated and a discrete sum is taken over a number of output modes. To form a complete basis or a total order

Table 2 Uncertainty sources and relevant information for the the 37.8 MJ/kg bulk enthalpy, 50 kpa total pressure condition with a 3.3-cm calibration probe.

No.	Description	Classification	Nominal	Uncertainty	Ref.
1	Dissociation reaction rate: N_2 + M ↔ 2N + M	Epistemic	1	±1 om	
2	Dissociation reaction rate: NO + M ↔ N + O + M	Epistemic	1	±1 om	
3	Dissociation reaction rate: O_2 + M ↔ 2O + M	Epistemic	1	±50%	West and Johnston [18]
4	Exchange reaction rate: N_2 + O ↔ NO + N	Epistemic	1	±50%	
5	Exchange reaction rate: O_2 + N ↔ NO + O	Epistemic	1	±1 om	
6	Binary collision integral: N_2-N_2	Epistemic	1	±20%	
7	Binary collision integral: N_2-O_2	Epistemic	1	±20%	
8	Binary collision integral: N_2-NO	Epistemic	1	±25%	
9	Binary collision integral: N_2-N	Epistemic	1	±20%	
10	Binary collision integral: N_2-O	Epistemic	1	±20%	
11	Binary collision integral: N_2-Ar	Epistemic	1	±20%	
12	Binary collision integral: O_2-O_2	Epistemic	1	±20%	
13	Binary collision integral: O_2-NO	Epistemic	1	±25%	
14	Binary collision integral: O_2-N	Epistemic	1	±25%	
15	Binary collision integral: O_2-O	Epistemic	1	±20%	Wright et al. [14]
16	Binary collision integral: O_2-Ar	Epistemic	1	±20%	Palmer [31]
17	Binary collision integral: NO-NO	Epistemic	1	±20%	
18	Binary collision integral: NO-N	Epistemic	1	±25%	
19	Binary collision integral: NO-O	Epistemic	1	±25%	
20	Binary collision integral: NO-Ar	Epistemic	1	±25%	
21	Binary collision integral: N-N	Epistemic	1	±5%	
22	Binary collision integral: N-O	Epistemic	1	±5%	
23	Binary collision integral: N-Ar	Epistemic	1	±20%	
24	Binary collision integral: O-O	Epistemic	1	±20%	
25	Binary collision integral: O-Ar	Epistemic	1	±20%	
26	Binary collision integral: Ar-Ar	Epistemic	1	±5%	
27	Nozzle catalytic recombination efficiency: N & O	Epistemic	1	-0.5, +1 om	Nawaz et al. [28]
28	Calibration probe catalytic recombination efficiency: N & O	Epistemic	1	-0.5, +1 om	
29	Arc heater current precision (amps)	Normal	345	3.9 sd	
30	Arc heater current bias error (amps)	Epistemic	0	±0.4	
31	Arc heater voltage precision (amps)	Normal	422	2.8 sd	
32	Arc heater voltage bias error (amps)	Epistemic	0	±2	
33	Plenum total pressure precision (kpa)	Uniform	50	±0.5	
34	Plenum total pressure bias error (kpa)	Epistemic	0	±0.2	
35	Arc water flow rate precision (gpm)	Normal	32.7	0.1 sd	
36	Arc water flow rate bias error (gpm)	Epistemic	0	±0.3	
37	Arc water temperature change precision (F)	Normal	13.4	0.4 sd	HyMETS calibration data
38	Arc water temperature change bias error (F)	Epistemic	0	±0.3	and instrument specs
39	Molecular nitrogen flow rate precision (slpm)	Normal	74.5	0.3 sd	
40	Molecular nitrogen flow rate bias error (slpm)	Epistemic	0	±1.5	
41	Molecular oxygen flow rate precision (slpm)	Normal	20.7	0.2 sd	
42	Molecular oxygen flow rate bias error (slpm)	Epistemic	0	±0.4	
43	Argon flow rate precision (slpm)	Normal	3.8	0.1 sd	
44	Argon flow rate bias error (slpm)	Epistemic	0	±0.1	
45	Calibration probe stagnation pressure precision (kpa)	Normal	2.81	0.01 sd	
46	Calibration probe stagnation pressure bias error (kpa)	Epistemic	0	±0.007	
47	Calibration probe stagnation heat flux bias (W/cm^2)	Epistemic	243.1	±10%	Nawaz and Santos [10]

expansion, N_t terms are required, which can be computed from Eq. (15) for a polynomial chaos expansion (PCE) of order q and a number of random dimensions or variables, n.

$$N_t = \frac{(n+q)!}{n!q!} \tag{15}$$

Further details on polynomial chaos theory are given by Eldred [35] and Ghanem [36]. Additionally, polynomial chaos expansions can be used to compute the Sobol indices, which are used to determine the contribution of each parameter to the total uncertainty [37]. In this study, Sobol indices are used to rank each parameter in terms of its contribution to the total variance of each stochastic response, R.

The objective with any PCE method is to determine the expansion coefficients, α_i. To do this, polynomial chaos methods can be implemented using an intrusive or a non-intrusive approach. While an intrusive method may appear straightforward in theory, for complex problems this process may be time consuming, expensive, and difficult to implement as changing the deterministic model is required [38]. In contrast, the non-intrusive approach can be easily implemented to construct a surrogate model that represents a complex computational simulation, because no modification to the deterministic model is required. The non-intrusive methods require only the response values at selected sample points to approximate the stochastic response surface.

Several methods have been developed for non-intrusive polynomial chaos (NIPC). Of these, the point-collocation NIPC method has been used extensively in many aerospace simulation and CFD problems [39–42] for improved computational efficiency and tractability for high-dimension problems over other spectral projection based approaches. The point-collocation method starts with replacing a stochastic response or random function with its PCE by using Eq. (14). Then, N_t sample vectors are chosen in random space and the deterministic code is evaluated at these points, which is the left hand side of Eq. (14). Following this, a linear system of N_t equations can be formulated and solved for the expansion coefficients of the PCE. This system is shown in Eq. (16).

$$\begin{pmatrix} R(\mathbf{D},\boldsymbol{\xi}_0) \\ R(\mathbf{D},\boldsymbol{\xi}_1) \\ \vdots \\ R(\mathbf{D},\boldsymbol{\xi}_P) \end{pmatrix} = \begin{pmatrix} \Psi_0(\boldsymbol{\xi}_0) & \Psi_1(\boldsymbol{\xi}_0) & \cdots & \Psi_P(\boldsymbol{\xi}_0) \\ \Psi_0(\boldsymbol{\xi}_1) & \Psi_1(\boldsymbol{\xi}_1) & \cdots & \Psi_P(\boldsymbol{\xi}_1) \\ \vdots & \vdots & \ddots & \vdots \\ \Psi_0(\boldsymbol{\xi}_P) & \Psi_1(\boldsymbol{\xi}_P) & \cdots & \Psi_P(\boldsymbol{\xi}_P) \end{pmatrix} \begin{pmatrix} \alpha_0 \\ \alpha_1 \\ \vdots \\ \alpha_P \end{pmatrix} \tag{16}$$

Note that for this linear system, N_t is the minimum number of deterministic samples required to obtain a direct solution. If more samples are available and are linearly independent, the system is considered overdetermined and can be solved using a least squares approach. The number of samples over the required minimum is represented by the use of an oversampling ratio (OSR), defined as the ratio of number of actual samples to the minimum number required (i.e., N_t).

In general, the number of collocation points can be determined by multiplying Eq. (15) by an OSR. Hosder et al. [43] determined that the PCE is dependent on the number of collocation points and an effective OSR of two was sufficient for the stochastic model problems studied.

B. Validation Approach

One approach to quantifying the difference between a model prediction and experimental data is the area metric proposed by Ferson et al. [44]. Shown in Eq. (17), d is the area between two cumulative distribution functions (CDF), F and S, which represent the probability distributions of a prediction and experimental measurements of x, respectively.

$$d(F, S) = \int_{-\infty}^{\infty} |F(x) - S(x)| dx \tag{17}$$

This metric is the measure of the evidence for disagreement between a prediction (or simulation) and an experiment. The value of the metric, $d(F, S)$, can also be viewed as the amount of model-form uncertainty that exists in the prediction. While the metric in Eq. (17) has many advantages and is very applicable to many engineering problems, there are cases when the metric breaks down. When epistemic and aleatory uncertainty exists in both the simulation and the experiment, Eq. (17) cannot be applied directly as it was only intended for cases with only aleatory uncertainty.

Oberkampf and Roy [45] proposed a metric for treating the case when both aleatory and epistemic uncertainty exist in the experiment and simulation. This formulation is shown in Eq. (18).

$$d(F, S) = \int_{-\infty}^{\infty} \Delta([F_R(x), F_L(x)], [S_R(x), S_L(x)]) dx \tag{18}$$

where,

$$\Delta(A, B) = \min_{\substack{a \in A \\ b \in B}} |a - b|$$

Here, the L and R subscripts denotes the left and right probability box boundaries (CDFs). This metric results in the area of non-overlap between the probability boxes and can be visualized in Figure 15. While this metric allows for both epistemic and aleatory uncertainty to exist in both the prediction and experiment, it still falls short in resolving true differences between the possible probability distributions contained within prediction and experimental data. With this approach, the metric d could potentially be independent of the amount of epistemic uncertainty in the measurements,

meaning that there are some instances where an increase or decrease in the epistemic uncertainty in the left or right bounds would have no change on d. For example, in Figure 15, if the measurement had a larger epistemic uncertainty due to an decrease in the left bound, the metric d would not change. Therefore, with this metric, two separate problems can result in the same model-form uncertainty even though one exhibits a larger amount of epistemic uncertainty.

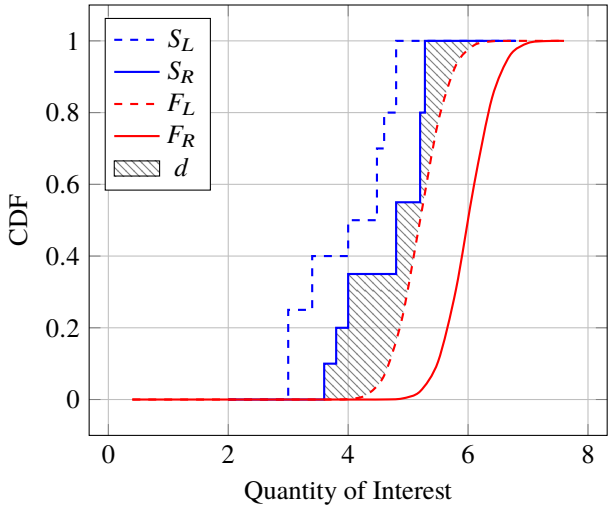

Fig. 15 Area metric given by Eq. (18)

To resolve the issues with the existing area metrics, a new area validation metric is proposed here. Keeping in line with previous approaches, the area metrics in Eqs. (17) and (18) can be extended to measure the disagreement between both the upper and lower bounding CDFs of the prediction and measurement. This results in two metrics, d_L and d_R, for left and right bounding CDFs, respectively, shown in Eq. (19).

$$d_L, d_R = \int_{-\infty}^{\infty} g_L(x)dx, \int_{-\infty}^{\infty} g_R(x)dx \tag{19}$$

where,

$$g_L(x) = \begin{cases} 0 & \text{for } x \text{ such that } F_L(x) \geq S_L(x) \\ S_L(x) - F_L(x) & \text{for } x \text{ such that } F_L(x) < S_L(x) \end{cases}$$

and

$$g_R(x) = \begin{cases} 0 & \text{for } x \text{ such that } F_R(x) \leq S_R(x) \\ F_R(x) - S_R(x) & \text{for } x \text{ such that } F_R(x) > S_R(x) \end{cases}$$

The resulting metrics d_L, d_R quantify the evidence for disagreement between both the left and right bounding probability distributions, while preserving the range of possible distributions from both the prediction and measurements. With this metric, the amount of epistemic uncertainty in the measurements is now accounted for in the metric values. There is still a possibility that one or both values could be zero. A zero value does not imply the two are in agreement, but rather suggests that there is no evidence for disagreement. Stated another way, the validation metric cannot represent a reduction in epistemic uncertainty of the simulation. The model-form uncertainty is independent of the input epistemic uncertainty and, therefore, is not reducible without calibrating the simulation inputs to the same known measurement inputs.

There is only one instance when both d_L and d_R could be zero. This is when the simulation bounds all of the experimental measurements, thereby capturing all of the possibilities within the domain of the uncertainties in the simulation. Note again, that the amount of epistemic uncertainty is not reducible by the value of the validation metric. The model-form uncertainty is zero given the current state of knowledge with regards to the simulation model-form uncertainty.

Figure 16 shows comparisons of the metric computed using Eqs. (18) and (19). The metric d computed using Eq. (18) results in the shaded region in Figure 16(a). This area is where the two probability boxes do not overlap. Notice that if the epistemic uncertainty on the right side of the probability box in the measurements was either more or less, this metric would remain constant. Using Eq. (19), d_L results in the shaded region shown in Figure 16(b). Note that d_R is zero in this case as the right CDF from the prediction is greater than that of the measurements. The metric d_L captures the possible distributions from the measurements.

Figure 17 shows two cases where the metric from Eq. (19) can be used to compute separate metrics for the left and right sides of the prediction distribution. In Figure 17(a), the measurements bound all of the predictions. Figure 17(b) is a case where the probability boxes from the prediction and measurements intersect. In both cases, d_L and d_R can be quantified with Eq. (19). Note that Eq. (18) would result in $d = 0$ for both of these cases as there is no evidence for disagreement based on that metric. The metric in Eq. (19) results in metrics that quantify the model-form uncertainty in the prediction given the knowledge-based uncertainty in the model.

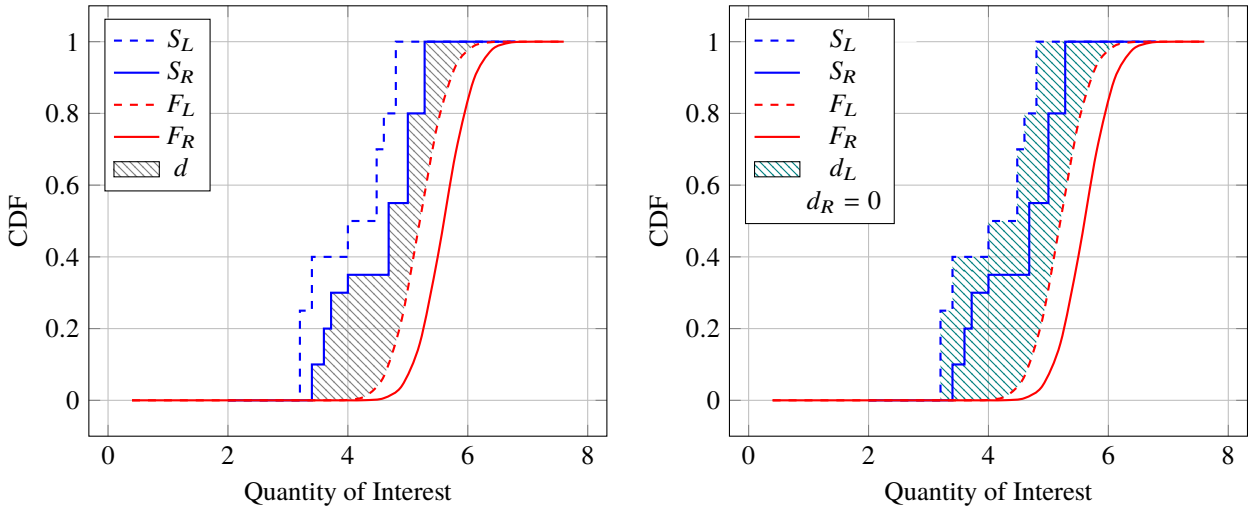

(a) Area metric using Eq. (18)

(b) Area metric using Eq. (19)

Fig. 16 Comparison of validation metrics computed given in Eq. (18) vs. Eq. (19) for a non-overlapping probability box case.

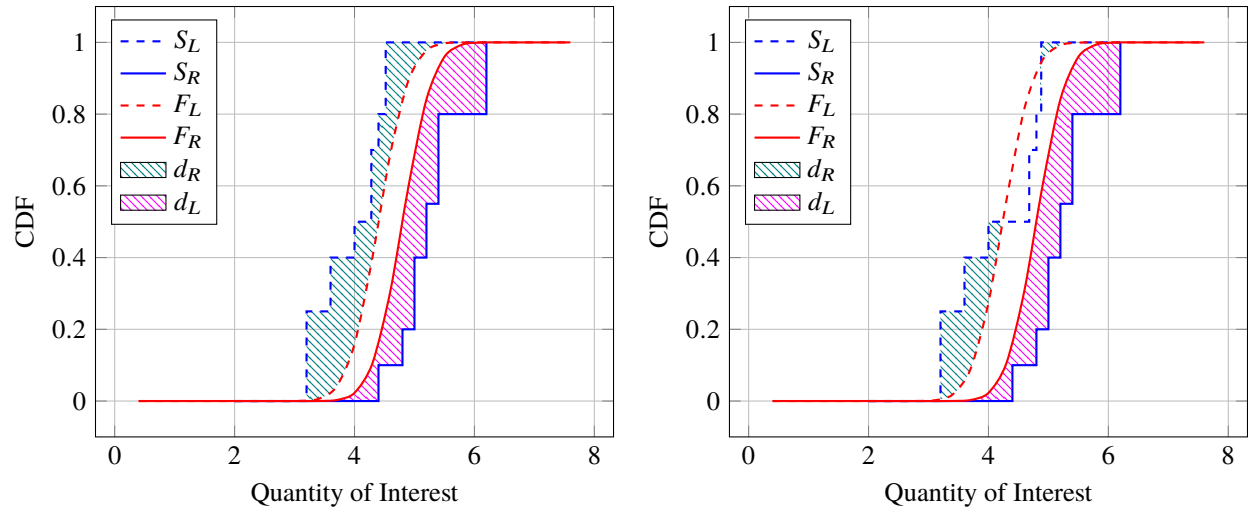

(a) Predictions contained within measurements.

(b) Predictions with partial overlap with measurements.

Fig. 17 Example cases with intersecting prediction and measurement probability boxes.

V. Results and Discussion

Recall from Section III that there are a total of 47 uncertain parameters considered in this study. Propagating the uncertainty with a second-order PCE requires a minimum of 1,176 evaluations of the CFD model to construct a second-order expansion from Eq. (15). The number of runs required is feasible in this study due to the limited computational cost of the model by perturbing the converged solution. This section presents the sensitivity results in identifying the main contributors to the total variance in the calibration probe heat flux and pressure predictions for

a low- and high-enthalpy condition. Then, a validation study is conducted by comparing the predictions to the data measured by the probes for both enthalpy conditions.

A. Sensitivity Analysis

Following the approach outlined in Section IV.A., a Latin hypercube sample structure of 1,500 samples was generated using all 47 uncertain variables. Using a least squares approach, a second-order polynomial chaos expansion was constructed for output response predictions of the stagnation-point heat flux and pressure of the calibration probe using 1,450 of the 1,500 samples with an oversampling ratio of approximately 1.25. To validate the accuracy of the surrogate model, a series of test points of the remaining 50 samples were used throughout the design space for comparison to the surrogate. On average, the surrogate model prediction was within 0.5% and 1.7% of the test points predicted by the CFD model for the stagnation-point pressure and heat flux, respectively. This result suggests that a second-order fit was adequate for this analysis, and the results for the sensitivities and uncertainty propagation are accurate.

Knowing the output variance of the predicted heat flux and pressure of the calibration probe is critical in understanding and ensuring appropriate conditions are tested on specimens in the facility. Given the amount of the uncertainty and how it compares to the measured test data, the output variation may be reduced by focusing on those parameters that contribute most significantly to the total output uncertainty. The aerosciences and measurement community would benefit from a sensitivity analysis of the predicted probe surface heat flux and pressure to the uncertain input parameters and whether these significant inputs come from the measurements recorded from the facility or the model inputs used to predict the environments. Based on the procedure outlined in Section IV.A, the global nonlinear sensitivities were evaluated for each uncertain parameter using the second-order expansion with all of the 1,500 samples. Those parameters that contribute more than 1% to the total uncertainty of the stagnation-point pressure and heat flux are shown in Table 3.

As discussed in Section III, there is a small amount of diatomic oxygen dissociation that is generated by the arc heater at a fairly low temperature of approximately 3500 K for the low-enthalpy condition; the dissociated gas remains vibrationally frozen through the nozzle expansion and the test cabin, prior to the calibration probe. A commonality among most of the top contributing parameters in Table 3 is the influence of these parameters on the total heating to the calibration probe surface. The bias uncertainty in the heat flux measurement, and the arc current and water temperature change uncertainty, impact the average enthalpy level and the peakness of the enthalpy profile at the nozzle exit, prior

Table 3 Contributions of the top uncertain parameters to the stagnation-point conditions of the calibration probe for the 5.5 MJ/kg bulk enthalpy, 103 kpa total pressure condition.

Uncertain Parameter	Stagnation-point Pressure	Stagnation-point Heat Flux
Binary collision integral: N_2-N_2	1.1%	3.7%
Binary collision integral: N_2-O_2	1.0%	9.2%
Binary collision integral: N_2-NO	<1%	2.0%
Binary collision integral: N_2-O	<1%	5.6%
Binary collision integral: N_2-Ar	<1%	1.1%
Calibration probe catalytic recombination efficiency: O	<1%	8.3%
Arc heater current precision	7.2%	1.2%
Arc water temperature change precision	15.1%	1.7%
Arc water temperature change bias error	5.1%	1.0%
Calibration probe stagnation heat flux bias	61.9%	54.7%

to the calibration probe. The impact in the enthalpy influences how much of the gas is dissociated in the arc heater and how much of the gas remains dissociated at the centerline of the nozzle. This level of dissociation dictates the potential of the catalytic heating to the surface of the calibration probe. As expected, these uncertain parameters that influence the freestream dissociation also greatly impact the freestream conditions upstream of the shock front, which is the primary cause for the stagnation-point pressure variability. For the low-enthalpy condition, improvements in the arc measurements, specifically the arc current and water temperature change, and the standard approach to calculate the stagnation-point heat flux of the calibration probe can lead to a reduction in the total variance of the probe surface predictions.

A paradigm shift was observed when assessing the sensitivities of the high-enthalpy condition. Table 4 presents the breakdown of the uncertain parameter contributions to the variance in the stagantion-point heat flux and pressure predictions. The results show that the uncertainty in the stagnation-point predictions are dominated by the uncertainty in the CFD model inputs for the high-enthalpy condition, which include the catalytic recombination efficiency of the atomic species present in the high-enthalpy flow, the O_2-N exchange reaction, and the collision integrals for the N_2-N_2, N_2-O_2, and N_2-O collision pairs. Each of these parameters contributes to a component of the total heat transfer to the nozzle and probe surfaces. In the case of the nozzle surface, these uncertainties impact the total heating removed from the flow and influences the magnitude of the enthalpy in the core flow in the test cabin, where the probes are inserted into the flow to take measurements. Figure 18 shows the impact of the catalytic efficiency in the nozzle to the magnitude of the total enthalpy at the nozzle exit, prior to the test cabin. While holding all other uncertainties constant, the uncertainty in the recombination of the atomic species in the nozzle can result in a total enthalpy change of up to 3 MJ/kg at the nozzle exit. The impact of the catalytic efficiency on the total enthalpy of the test gas explains why

contributions related to the heat transfer in the nozzle in Table 4 can have an impact on not only the predicted heat flux, but also the predicted stagnation pressure.

Table 4 Contributions of the top uncertain parameters to the stagnation-point conditions of the calibration probe for the 37.8 MJ/kg bulk enthalpy, 50 kpa total pressure condition.

Uncertain Parameter	Stagnation-point Pressure	Stagnation-point Heat Flux
Exchange reaction rate: $O_2 + N \leftrightarrow NO + O$	44.2%	23.3%
Binary collision integral: N_2-N_2	3.2%	1.3%
Binary collision integral: N_2-O_2	7.5%	1.6%
Binary collision integral: N_2-O	6.7%	3.9%
Nozzle catalytic recombination efficiency: N & O	35.5%	15.4%
Calibration probe catalytic recombination efficiency: N & O	<1%	49.1%

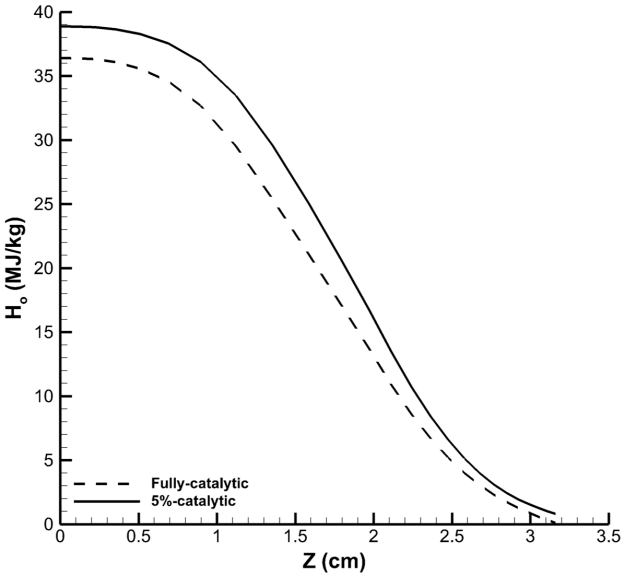

Fig. 18 Total enthalpy radial profiles at the nozzle exit as a function of catalytic efficiency in the nozzle for the 37.8 MJ/kg bulk enthalpy, 50 kpa total pressure condition.

For both low- and high-enthalpy conditions, there are some improvements that can be made in the CFD model inputs used to predict the probe surface heat flux and pressure, which include the binary collision processes in calculating the transport properties and the catalytic recombination efficiency of the probe surface and nozzle. As discussed in Section III, the community typically assumes the copper surfaces to be fully-catalytic; however, this may only be particularly true if the copper is exposed in an oxgyen-free environment. According to studies by Nawaz et al. [28], the copper surface can oxidize in a short period of time to form cuprous or cupric oxide in a room temperature molecular oxygen environment; cuprous or cupric oxide can also form on the surface during arc-jet tests involving some level of oxygen. The level of discoloration is typically one indicator that the copper surface has oxidized. In order to mitigate the

uncertainty in this oxidation process that impacts the catalytic nature of the nozzle and the calorimeters used to measure the heat flux, investments should be made in developing an appropriate catalytic model for the copper surfaces in the HyMETS facility. The catalytic models are typically formulated as a function of surface temperature for TPS practices, but the calibration probe is only exposed for a short period of time at a relatively cold surface temperature; therefore, the catalysis model development should be focused at a cold-wall condition while varying the pressure environments of the facility envelope in which the probe will be exposed to. The partial pressures of the oxygen, in the case of the calorimeter probe, will be the dominating impact to the catalytic behavior of the probe surface. The models developed for the copper probes can be used to inform the catalytic behavior of the nozzle, which is water-cooled to maintain surface temperatures near room temperature. For both conditions, the collision pairs that include N_2 also significantly influence the heating uncertainty at the nozzle and probe surfaces. Although not a large driver in the total variance of the stagnation predictions compared to the catalytic efficiencies, considerations should be made in reassessing accuracies of the collision integral fits for these significant pairs that span the facility performance envelope of HyMETS.

B. Uncertainty Propagation and Statistical Validation

The second-order expansion surrogate models for each of the arc heater conditions, constructed in the previous subsection to evaluate the sensitivities, was also used to determine the uncertainty in the stagnation-point predictions of the calibration probe and compare the predictions to available calorimetry data. The uncertainty was propagated through the surrogate models for both the stagnation-point heat flux and pressure via Monte Carlo sampling with 1.6 million samples.

Figure 19 shows the probability box plots of the stagnation-point probe surface predictions compared to the uncertainty in the stagnation-point probe measurements for the low-enthalpy condition. The prediction uncertainty, quantified by the constructed surrogate models, is repsesented by the bounding blue lines, and the experimental uncertainty, measured by the calibration probes, is represented by the bounding red lines, which reflects the probe measurement uncertainties reported in Table 1. The stagnation-point pressure prediction varies as much as 600 Pa, while the stagnation-point heat flux varies as much as 25 W/cm^2. These uncertainties in the stagnation-point predictions are primarily driven by the input uncertainties identified in the previous subsection (Table 3). The results also show evidence of statistical disagreement, where the stagnation-point pressure and heat flux predicted by CFD do not intersect the possible calibration probe measurements at higher values.

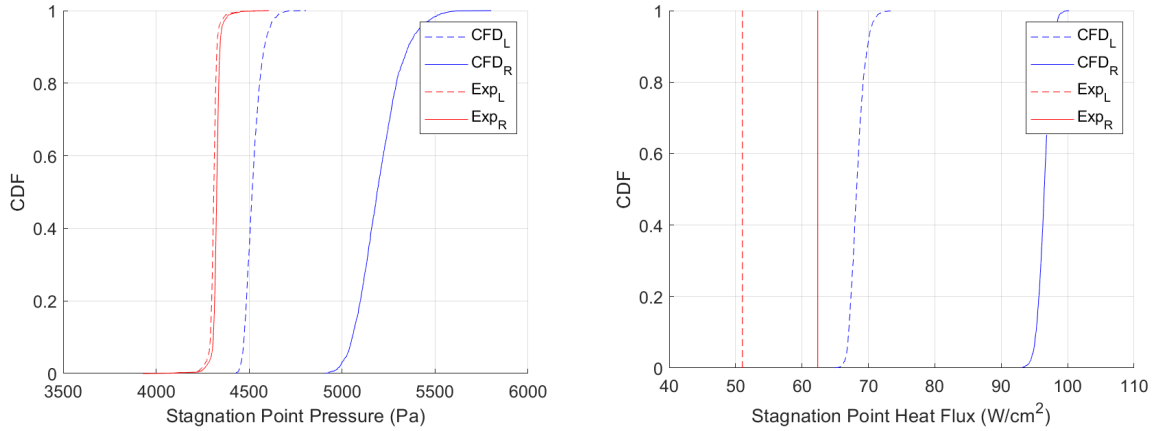

(a) Stagnation-point surface pressure.

(b) Stagnation-point convective heat flux.

Fig. 19 Uncertainty in probe surface predictions compared with measurement uncertainty for the low-enthalpy condition.

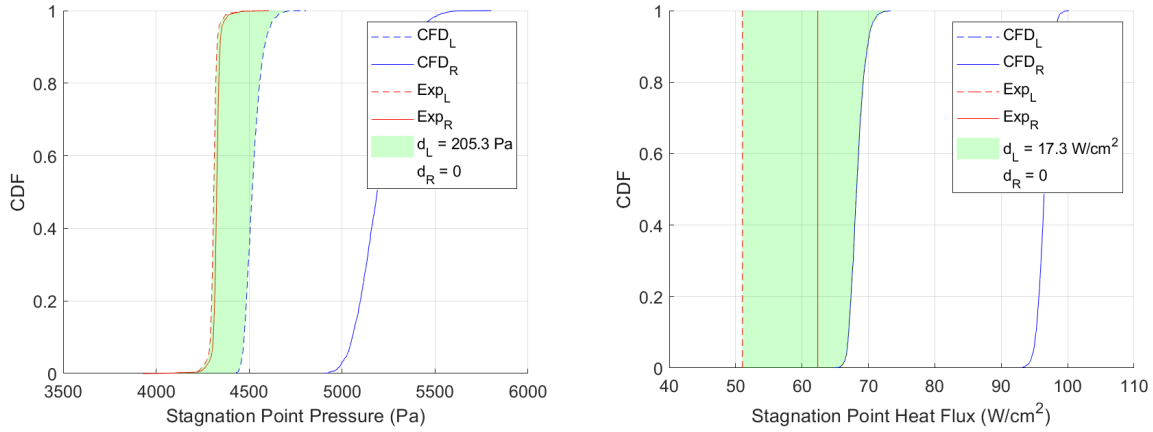

(a) Stagnation-point surface pressure.

(b) Stagnation-point convective heat flux.

Fig. 20 Calculation of the validation metric for the probe surface predictions for the low-enthalpy condition.

The results presented in Figure 19 are a special case of resemblance to those shown by Figure 16(b) in Section IV.B. Applying Eq. (19) in Figure 20, $d_R = 0$ as the upper bound of the simulation CDF is greater than that of the measurements. However, the possible distributions from the measurement are not contained by the prediction uncertainty, so a validation metric, d_L, is computed between the lower-bound CDFs of the prediction and measurement. The results in Figure 20 show that the left CDF of the prediction uncertainty for the stagnation-point pressure and heat flux should be padded by an additional 205.3 Pa and 17.3 W/cm^2, respectively, which is indicated by the area shaded in green. This additional uncertainty added to the prediction accounts for model-form uncertainty that is not precisely known with the current state of knowledge of the epistemic model-form uncertain inputs of the simulation.

Figure 21 shows the probability box plots of the stagnation-point probe surface predictions compared to the uncertainty in the stagnation-point probe measurements for the high-enthalpy condition. At this higher energy condition in the arc jet, the uncertainty in predictions are represented as purely epistemic intervals because of the paradigm shift in significant contributions towards CFD model-form uncertain inputs. In Figure 21, the results show that there is no evidence of disagreement between the predictions and measurements of the stagnation-point pressure; therefore, no validation metric is needed because all of the possible measurements are contained within the prediction uncertainty, as shown in Figure 22. However, the prediction uncertainty is quite large compared to the measurement uncertainty. The uncertainty in the stagnation-point pressure prediction varies as much as approximately 2500 Pa, because the uncertainty in catalytic efficiency in the nozzle, the associated exchange reaction of O_2-N, and the binary collision interactions involving N_2 affect the amount of heat transfer out of the flow in the nozzle. The amount of heat transfer in the nozzle affects the freestream condition in the test cabin prior to the calibration probe, thus resulting in large variations in the stagnation-point pressure prediction. A similar rationale can made for the stagnation-point heat flux prediction uncertainty in the Figure 21, which varies as much as approximately 300 W/cm^2. However, the catalytic recombination efficiency at the probe surface becomes a significant contributor to the variance in the heat flux prediction. Similar to the low-enthalpy condition, an area validation metric of 40.8 W/cm^2 is needed to account for evidence of disagreement on the left bounding CDF of the stagnation-point heat flux prediction. This additional padding to the left bounding CDF assures that the possible measured values of the stagnation-point heat flux are contained within the uncertainty in the stagnation-point heat flux prediction.

The results shown for the performance envelope of the HyMETS facility illustrate that the pressure predictions require little-to-no validation padding to account for all possible pressure measurements by the Pitot probe. Alternatively, the heat flux predictions tend to over-predict most of the possible measurements by the slug calorimeter, and therefore, requires a left-leaning validation adjustment to account for the possible heat flux measured values. This also applies to analyses with similar arc-heater conditions (e.g. bulk enthalpy, arc heater settings, and mass flow rate) in which the validation metric, d_L, should be accounted in the prediction uncertainty in the absence of test data, because it is not reducible with the present knowledge of uncertainty in the inputs used. However, the validation metric can be reassessed if additional knowledge is acquired to modify the uncertainty in the significant uncertain inputs identified

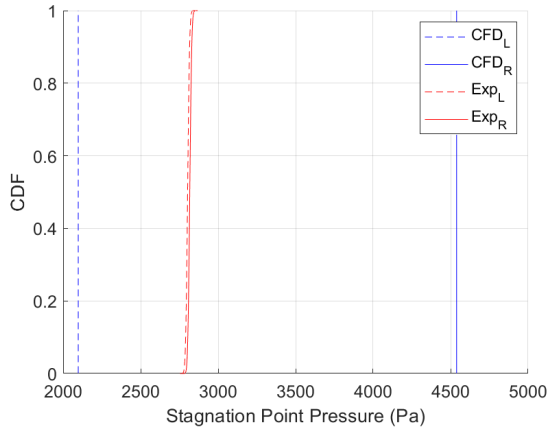

(a) Stagnation-point surface pressure.

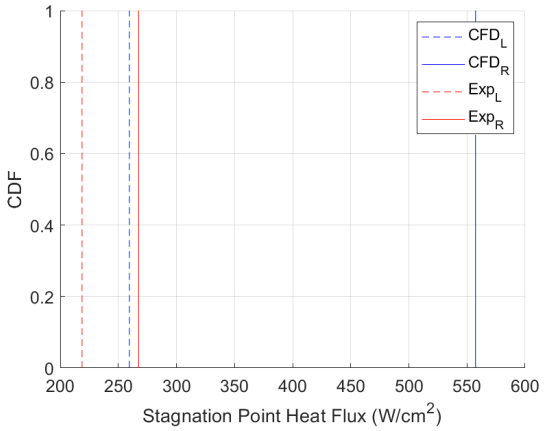

(b) Stagnation-point convective heat flux.

Fig. 21 Uncertainty in probe surface predictions compared with measurement uncertainty for the high-enthalpy condition.

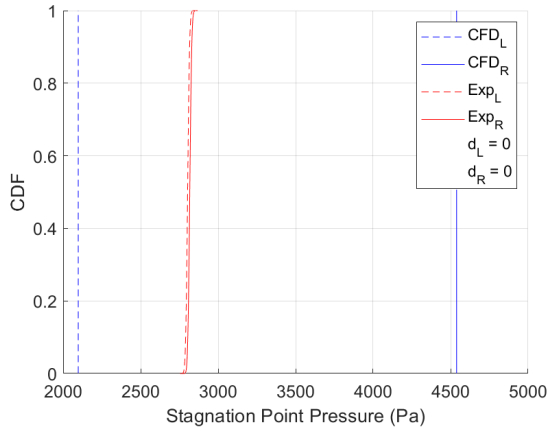

(a) Stagnation-point surface pressure.

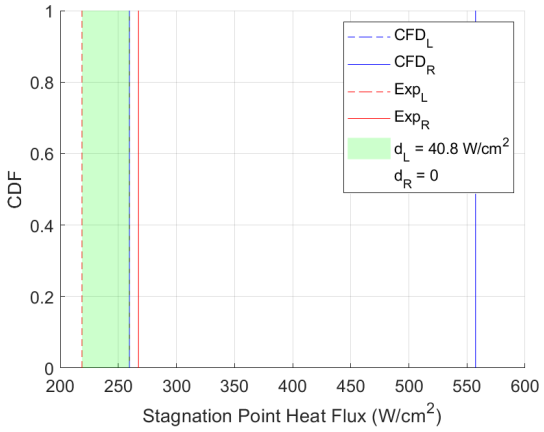

(b) Stagnation-point convective heat flux.

Fig. 22 Calculation of the validation metric for the probe surface predictions for the high-enthalpy condition.

in the previous subsection. More specifically, there are some notable improvements to be made that can reduce the evaluated validation metrics (i.e., model-form uncertainty).

First and foremost, discussion in the literature indicates that the accuracy in the calculated heat flux from the measured temperature data on the backface of the slug calormimeter can be improved by accouting for thermal losses from the slug [9, 10]. In addition, an in-depth analysis of the spread in temperature response on the backface of the slug can aid in re-evaluating the bias in the heat flux measurement. (Recall that an adopted $\pm 10\%$ uncertainty has been used in this study [28].) Another issue that could the explain the evidence for disagreement between heat flux measurement and prediction is the catalytic recombination efficiency of the copper surfaces in the nozzle and on the probe surface. The catalytic behavior of the copper surfaces can be complicated with the potential oxidation in arc flows with available oxygen, and the uncertainties in the catalytic recombination efficiencies for these probe surfaces are not well-defined. Furthermore, Brune et al. [3] studied similar conditions in previous work with reported heat flux values that were much higher than those reported in this study from recent calibration runs in HyMETS, which could explain the reasoning for the disagreement between prediction and measurement. Additional diagnostics are needed in evaluating the accuracy of the calculated heat flux values and the consistency in heat flux readings from the facility in relation to the surface characterization of the probes used. The authors will work towards these efforts in a future study to better understand these environments on the slug calorimeters.

VI. Conclusions

An uncertainty analysis of the stagnation-point calibration probe surface predictions was presented for a low- and high-enthalpy condition that span the performance envelope of the Hypersonic Materials Environmental Test System facility. The analysis in this study accounts for the precision and bias uncertainties in the measurements and epistemic uncertainties in the computational fluid dynamics model used to predict the stagnation-point pressure and heat flux of the calibration probe. The calibration probe predictions were ccompared to measured data for a deterministic set of arc heater conditions to demonstrate the need to assess the uncertainty, and determine if there is statistical agreement, in the stagnation-point predictions and measurements. Uncertainty sources were identified and discussed based on available references and test data to formulate the uncertain ranges and classification.

Given the limited expense of the computational fluid dynamics model used in this study, a surrogate-based approach using non-intrusive polynomial chaos was applied to construct a response surface for the stagnation-point heat flux

and pressure with 47 uncertain parameters. The response surfaces were then used to conduct a sensitivity analysis, propagate the uncertainty, and compare the prediction uncertainty to the measurement uncertainty. Sensitivity results showed that the measurement bias uncertainty is the most significant contributor to the stagnation-point pressure and heat flux variance for the low-enthalpy condition. More specifically, the calibration probe heat flux bias and arc water temperature precision/bias accounted for most of the stagnation-point pressure variance, while the calibration probe heat flux bias, catalytic recombination efficiency, and binary collision pairs with molecular nitrogen significantly influenced the total variance in the stagnation-point heat flux. A shift in sensitivities was observed for the high-enthalpy condition; computational fluid dynamics model input associated with the catalytic efficiency in the nozzle and on the probe surface, and the O_2-N exchange reaction rate were main contributors to the uncertainty in the stagnation-point probe predictions.

The significant uncertain parameters for the low-enthalpy condition resulted in a stagnation-point pressure and heat flux uncertainty of about 600 Pa and 25 W/cm^2, respectively. For the high-enthalpy condition, the variability in the predictions were much larger due to the influence in highly-dissociated flow on the freestream envrionments in the test cabin and the catalytic recombination to the probe surface. A comparison between the probability box plots of the prediction and measurement uncertainty showed that there is little-to-no evidence of statistical disagreement for the stagnation-point pressure; however, disagreement between prediction and measurement was observed for the stagnation-point heat flux, where the prediction uncertainty overpredicts the measurement uncertainty. A validation metric was proposed in this study and applied to the prediction uncertainty to account for the statistical disagreement between the prediction and measurement of the stagnation-point heat flux and pressure.

References

[1] Prabhu, D., Saunders, D., Oishi, T., Skokova, K., Sanots, J., Fu, J., Terrazas-Salinas, I., Carballo, E., and Driver, D., "CFD Analysis Framework for Arc-Heated Flowfields, I: Stagnation Testing in Arc-Jets at NASA ARC," AIAA 2009-4080, June 2009.

[2] Mazaheri, A., Bruce, W., Mesick, N., and Sutton, K., "Methodology for Flight-Relevant Arc-Jet Testing of Flexible Thermal Protection Systems," *Journal of Spacecraft and Rockets*, Vol. 51, No. 3, 2014, pp. 789–800.

[3] Brune, A., Bruce, W., Glass, D., and Splinter, S., "Computational Simulations of the NASA Langley HyMETS Arc-Jet Facility," Tech. rep., NASA NF1676L-28439, 2017.

[4] Splinter, S., Bey, K., and Gragg, J., "Comparative Measurements of Earth and Martian Entry Environments in the NASA Langley HyMETS Facility," AIAA 2011-1014, Jan. 2011.

[5] Wiedemann, K., Clark, R., and Sankaran, S., "Emittance, Catalysis, and Dynamic Oxidation of Ti-14AL-21Nb," Tech. rep., NASA TP-2955, Nov. 1989.

[6] Glass, D., "Oxidation and Emittance Studies of Coated Mo-Re," Tech. rep., NASA CR-201753, Oct. 1997.

[7] Bird, R., Wallace, T., and Sankaran, S., "Development of Protective Coatings for High-Temperature Metallic Materials," *Journal of Spacecraft and Rockets*, Vol. 41, No. 2, 2004, pp. 213–220.

[8] Calomino, A., Bruce, W., Gage, P., Horn, D., Mastaler, M., Rigali, D., Robey, J., Voss, L., Wahlberg, J., and Williams, C., "Evaluation of the NASA Arc-Jet Capabilities to Support Mission Requirements," Tech. rep., NASA SP-2010-577, Nov. 1989.

[9] American Society for Testing Materials (ASTM), ., "Standard Test Method for Measuring Heat-Transfer Rate Using a Thermal Capacitance (Slug) Calorimeter," Tech. rep., ASTM Standard E457-96, 1996.

[10] Nawaz, A. and Santos, J., "Assessing Calorimeter Evaluation Methods in Convective and Radiative Heat Flux Environment," AIAA 2010-4905, June 2010.

[11] American Society for Testing Materials (ASTM), ., "Standard Practice for Measuring Plasma Arc Gas Enthalpy by Energy Balance," Tech. rep., ASTM Standard E341-81, 1981.

[12] Park, C., "Review of Chemical-Kinetic Problems of Future NASA Missions, I: Earth Entries," *Journal of Thermophysics and Heat Transfer*, Vol. 7, No. 3, 1993, pp. 385–398.

[13] Gupta, R., Yos, J., Thompson, R., and Lee, K., "A Review of Reaction Rates and Thermodynamic and Transport Properties for an 11-Species Air Model for Chemical and Thermal Nonequilibrium Calculations to 30,000 K," Tech. rep., NASA RP-1232, 1990.

[14] Wright, M., "Recommended Collision Integrals for Transport Property Computations Part 1: Air Species," *AIAA Journal*, Vol. 43, No. 12, 2005, pp. 2558–2564.

[15] Wright, M., "Recommended Collision Integrals for Transport Property Computations Part 2: Mars and Venus Entries," *AIAA Journal*, Vol. 45, No. 1, 2005, pp. 281–288.

[16] Gordon, S. and McBride, B., "Computer Program for Calculation of Complex Equilibrium Compositions and Applications," Tech. rep., NASA RP-1311, 1994.

[17] Brune, A., West, T., Hosder, S., and Edquist, K., "Uncertainty Analysis of Mars Entry Flows over a Hypersonic Inflatable Aerodyanmic Decelerator," *Journal of Spacecraft and Rockets*, Vol. 52, No. 3, 2015, pp. 776–788.

[18] West, T. and Johnston, C. O., "Uncertainty and Sensitivity Analysis of Afterbody Radiative Heating Predictions for Earth Entry," *Journal of Thermophysics and Heat Transfer*, Vol. 31, No. 2, 2017, pp. 294–306.

[19] Hash, D., Olejniczak, J., Wright, M., Prabhu, D., Pulsonetti, M., Hollis, B., Gnoffo, P., Barnhardt, M., Nompelis, I., and Candler, G., "Fire II Calculations for Hypersonic Nonequilibrium Aerothermodynamics Code Verification: DPLR, LAURA, and US3D," AIAA 2007-0605, Jan. 2007.

[20] Mazaheri, M. and Wood, W., "Re-Entry Aeroheating Analysis of Tile-Repair Augers for the Shuttle Orbiter," AIAA 2007-4148, June 2007.

[21] Mazaheri, A. and Wood, W., "Heating Augmentation for Short Hypersonic Protuberances," *Journal of Spacecraft and Rockets*, Vol. 46, No. 2, 2009, pp. 284–291.

[22] Dyakonov, A., Schenenberger, M., Scallian, W., Van Norman, J., Novak, L., and Tang, C., "Aerodynamic Interference Due to MSL Reaction Control System," AIAA 2009-1030, Jan. 2009.

[23] Johnston, C., Gnoffo, P., and Mazaheri, A., "A Study of Ablation-Flowfield Coupling Relevant to the Orion Heatshield," AIAA 2009-4318, June 2009.

[24] Mazaheri, A., "HEART Aerothermodynamic Analysis," Tech. rep., NASA TM-2012-217568, 2012.

[25] Smith, D. and Carver, D., "Flow Calibration of Two Hypersonic Nozzles in the AEDC Heat-H2 High-Enthalpy Arc-Heated Wind Tunnel," AIAA 1993-2782, 1993.

[26] Heister, N. and Clark, C., "Feasibility of Standard Evaluation Procedures for Ablating Materials," Tech. rep., NASA CR-379, 1966.

[27] Heister, N. and Clark, C., "Comparative Evaluation of Ablating Materials in Arc Plasma Jets," Tech. rep., NASA CR-1207, 1968.

[28] Nawaz, A., Driver, D., Terrazes-Salinas, I., and Sepka, S., "Surface Catalysis and Oxidation on Stagnation Point Heat Flux Measurements in High Enthalpy Arc Jets," AIAA 2013-3138, 2013.

[29] Johnston, C. O. and Panesi, M., "Advancements in Afterbody Radiative Heating Simulations for Earth Entry," AIAA 2016-3693, 2016.

[30] Bose, D., Wright, M., and Gokcen, T., "Uncertainty and Sensitivity Analysis of Thermochemical Modeling for Titan Atmospheric Entry," AIAA 2004-2455, 2004.

[31] Palmer, G., "Uncertainty Analysis of CEV LEO and Lunar Return Entries," AIAA 2007-4253, 2007.

[32] Bose, D., Wright, M., and Palmer, G., "Uncertainty Analysis of Laminar Aeroheating Predictions for Mars Entries," *Journal of Thermophysics and Heat Transfer*, Vol. 20, No. 4, 2006, pp. 652–662.

[33] Eldred, M. and Swiler, L., "Efficient Algorithms for Mixed Aleatory-Epistemic Uncertainty Quantification with Application to Radiation-Hardened Electronics," *Sandia National Laboratories Report*, Vol. SAND2009-5805, Sept. 2009.

[34] Xiu, D. and Karniadakis, G. E., "The Wiener–Askey Polynomial Chaos for Stochastic Differential Equations," *SIAM Journal on Scientific Computing*, Vol. 24, No. 2, 2002, pp. 619–644.

[35] Eldred, M. S., "Recent Advances in Non-Intrusive Polynomial Chaos and Stochastic Collocation Methods for Uncertainty Analysis and Design," AIAA Paper 2009-2274, May 2009.

[36] Ghanem, R. G. and Spanos, P. D., *Stochastic Finite Elements: A Spectral Approach*, Springer-Verlag, New York, 1991.

[37] Sudret, B., "Global sensitivity analysis using polynomial chaos expansion," *Reliability Engineering and System Safety*, Vol. 93, No. 7, 2008, pp. 964–979.

[38] Hosder, S. and Bettis, B., "Uncertainty and sensitivity analysis for reentry flows with inherent and model-form uncertainties," *Journal of Spacecraft and Rockets*, Vol. 49, No. 2, 2012, pp. 193–206.

[39] Bettis, B., Hosder, S., and Winter, T., "Efficient Uncertainty Quantification in Multidisciplinary Analysis of a Reusable Launch Vehicle," AIAA Paper 2011-2393, April 2011.

[40] Hosder, S., Walters, R. W., and Balch, M., "Point-Collocation Nonintrusive Polynomial Chaos Method for Stochastic Computational Fluid Dynamics," *AIAA Journal*, Vol. 48, No. 12, 2010, pp. 2721–2730.

[41] Han, D. and Hosder, S., "Inherent and Model-Form Uncertainty Analysis for CFD Simulation of Synthetic Jet Actuators," AIAA Paper 2012-0082, Jan. 2012.

[42] West IV, T. K., Hosder, S., and Johnston, C. O., "Multi-Step Uncertainty Quantification Approach Applied to Hypersonic Reentry Flows," *Journal of Spacecraft and Rockets*, Vol. 51, No. 1, 2014, pp. 296–310.

[43] Hosder, S., Walters, R. W., and Balch, M., "Efficient Sampling for Non-Intrusive Polynomial Chaos Applications with Multiple Uncertain Input Variables," AIAA Paper 2007-0125, 2007.

[44] Ferson, S., Oberkampf, W. L., and Ginzburg, L., "Model validation and predictive capability for the thermal challenge problem," *Computer Methods in Applied Mechanics and Engineering*, Vol. 197, No. 29, 2008, pp. 2408–2430.

[45] Oberkampf, W. L. and Roy, C. J., *Verification and Validation in Scientific Computing*, Cambridge University Press, New York, 2012.

[46] Giaquinta, M. and Modica, G., *Mathematical Analysis: Linear and Metric Structures and Continuity*, Birkhauser, Boston, 2007.